THE UNIVERSITY OF MANITOBA

THE ELASTODYNAMIC ANALYSIS OF CRACKS UNDER AXISYMMETRIC CONDITIONS BY A PATH-INDEPENDENT INTEGRAL

By

DOUGLAS ARTHUR SCARTH

A Thesis
Submitted to the Faculty of Graduate Studies
in Partial Fulfillment of the Requirements for the
Degree of Master of Science

Department of Mechanical Engineering

Winnipeg, Manitoba

May 1982

THE ELASTODYNAMIC ANALYSIS OF CRACKS UNDER AXISYMMETRIC CONDITIONS BY A PATH-INDEPENDENT INTEGRAL

BY

DOUGLAS ARTHUR SCARTH

A thesis submitted to the Faculty of Graduate Studies of the University of Manitoba in partial fulfillment of the requirements of the degree of

MASTER OF SCIENCE

© 1982

Permission has been granted to the LIBRARY OF THE UNIVERSITY OF MANITOBA to lend or sell copies of this thesis, to the NATIONAL LIBRARY OF CANADA to microfilm this thesis and to lend or sell copies of the film, and UNIVERSITY MICROFILMS to publish an abstract of this thesis.

The author reserves other publication rights, and neither the thesis nor extensive extracts from it may be printed or otherwise reproduced without the author's written permission.

ABSTRACT

A technique is developed for obtaining numerically the dynamic stress intensity factor for stationary cracks under axisymmetric mode I conditions in linear structures. This technique is based on the formulation of a path-independent integral, $J_{rg}(t)$, which describes the energy flux to the crack tip for a general class of axisymmetric mode I loading conditions. This integral is shown to be related to the dynamic stress intensity factor at the crack tip. An existing finite element computer code was modified to simulate wave propagation in linear elastic solids, and subsequently to evaluate the $J_{rg}(t)$-integral. Results from numerical examples are compared with those from other solutions. A practical case involving a thick-walled cylinder containing an inner-circumferential edge crack is presented. The numerically computed values of the dynamic stress intensity factor from $J_{rg}(t)$ are approximately independent of the path of integration. As well, the maximum values of the dynamic stress intensity factor are in close agreement with those from the other solutions. The results indicate that in using the $J_{rg}(t)$-integral a detailed knowledge of crack-tip conditions is not required a priori, allowing this technique to be convenient and economical to use.

ACKNOWLEDGEMENTS

The author wishes to express his appreciation for the guidance and help given by his academic advisor, Dr. T. R. Hsu.

The author wishes to acknowledge gratefully Dr. N. Popplewell for his valuable advice and suggestions. The author also wishes to express appreciation to Dr. J. Shewchuk and Dr. B. Pinkney for their valuable suggestions. Thanks go to Mrs. K. Nedohin for typing the manuscript.

The financial support from the Natural Sciences and Engineering Research Council of Canada and from Manitoba Hydro is gratefully acknowledged.

TABLE OF CONTENTS

	PAGE
ABSTRACT	i
ACKNOWLEDGEMENTS	ii
LIST OF FIGURES	vi
NOMENCLATURE	x
CHAPTER ONE - INTRODUCTION	1
1.1 Review of Elastodynamic Analyses of Stationary Cracks	2
1.2 Scope of Thesis	6
CHAPTER TWO - A GENERAL PATH-INDEPENDENT ENERGY-FLUX INTEGRAL FOR STATIONARY CRACKS UNDER AXISYMMETRIC MODE I CONDITIONS	7
2.1 Introduction	7
2.2 Review of Path-Independent Energy-Flux Integrals	8
2.3 Physical Model	10
2.4 Energy Flux into the Fracture-Process Region	14
2.5 Energy Flux Expressed as a Path-Independent Integral	18
2.6 Reduction of Surface and Volume Integrals	24
2.7 Limiting Cases	26
2.8 Relation with Dynamic Stress Intensity Factor	27
2.9 Conclusions	29

PAGE

CHAPTER THREE - FINITE ELEMENT ANALYSIS OF WAVE PROPAGATION IN LINEAR ELASTIC SOLIDS 30

3.1 Introduction 30

3.2 Discretized Equations of Motion 31

3.3 Direct Time-Integration of the Equations of Motion 36

3.4 Initial Conditions and Applied Loads . . . 38

3.5 Matrix-Decomposition Equation Solver . . . 38

CHAPTER FOUR - EXAMPLE PROBLEMS 40

4.1 Wave Propagation in Smooth Solids 40

4.1.1 Case 1: A Long Thick-Walled Cylinder Subjected to a Sudden Internal Pressure 40

4.1.2 Case 2: A Solid Cylinder Subjected to a Sudden End Loading 44

4.1.3 Case 3: A Semi-Infinite Half-Space Subjected to a Triangular Load 53

4.2 Axisymmetric Elastodynamic Crack Problems 60

4.2.1 Case 4: A Solid Cylinder Containing a Suddenly Pressurized Penny-Shaped Crack 61

4.2.2 Case 5: A Thick-Walled Cylinder Containing an Inner-Circumferential Edge Crack, Subjected to Sudden End Loadings 69

4.2.2a Application of the $J_{rg}(t)$-integral 71

4.2.2b Application of the Linear Extrapolation Technique 74

4.2.2c Results and Discussion 77

PAGE

CHAPTER FIVE - CONCLUSIONS AND RECOMMENDATIONS 84

REFERENCES 86

APPENDIX I FORMULATION OF EQUATION (2.18) 94

APPENDIX II PARTIAL DERIVATIVE OF ELASTIC STRAIN ENERGY DENSITY FUNCTION WITH RESPECT TO r 96

APPENDIX III INTEGRATION OF $\int_A \frac{\partial W}{\partial r} \frac{r}{a} dA$ BY PARTS . . 97

APPENDIX IV EXPRESSION OF EQUATION (2.27) IN TERMS OF STRESS TENSOR COMPONENTS . . . 99

APPENDIX V FINITE ELEMENT LUMPED-MASS MATRIX . . . 102

APPENDIX VI CALCULATION OF $K_I(t)$ BY THE LINEAR EXTRAPOLATION TECHNIQUE 105

LIST OF FIGURES

		PAGE
Figure 1.1	A coordinate system at the crack tip . .	4
Figure 2.1	Line-crack configuration	11
Figure 2.2	Cracked-cylinder segment containing a control volume	13
Figure 2.3	Illustration of the surface enclosing the control volume	15
Figure 3.1	A typical triangular finite element . .	32
Figure 4.1	An internally pressurized thick-walled circular cylinder	42
Figure 4.2	Variation of the normalized hoop stress, $\sigma_{\theta\theta}/P_o$, with non-dimensionalized time at the nominal radius $r = r_1$ in the internally pressurized thick-walled cylinder	43
Figure 4.3	A solid circular cylinder subjected to an end loading	45
Figure 4.4	Dependence of end loading on the solid cylinder on non-dimensionalized time	45
Figure 4.5	Variation of the normalized axial stress, σ_{zz}/P_o , with non-dimensionalized time at the nominal radius $r = 0$ in the solid cylinder . .	46

PAGE

Figure 4.6 Variation of the normalized axial stress, σ_{zz}/P_o, with non-dimensionalized time at the nominal radius $r = r_2$ in the solid cylinder 47

Figure 4.7 Variations of the normalized radial stress, σ_{rr}/P_o, and the normalized hoop stress, $\sigma_{\theta\theta}/P_o$, with non-dimensionalized time at the nominal radius $r = 0$ in the solid cylinder . 50

Figure 4.8 Variation of the normalized hoop stress, $\sigma_{\theta\theta}/P_o$, with non-dimensionalized time at the nominal radius $r = r_2$ in the solid cylinder 51

Figure 4.9 Variation of the normalized axial stress, σ_{zz}/P_o, along the nominal radius $r = r_2$ in the solid cylinder at $c_1 t/L = 1.0$ 52

Figure 4.10 A semi-infinite half-space subjected to a triangular load 54

Figure 4.11 Finite element model of the semi-infinite half-space 55

Figure 4.12 Variations of the normalized cartesian stress components, $\sigma_{ij}/|P_o|$, along $y = 2L$ in the semi-infinite half-space at the non-dimensionalized time $c_1 t/L = 6.0$ 57

PAGE

Figure 4.13 Variations of the normalized stresses $\sigma_{xx}/|P_o|$, $\sigma_{yy}/|P_o|$ and $\tau_{max}/|P_o|$ with non-dimensionalized time at $x = 0$ and $y = 2L$ in the semi-infinite half-space 58

Figure 4.14 Variations of the normalized cartesian stress components, $\sigma_{ij}/|P_o|$, with non-dimensionalized time at $x = 2L$ and $y = 2L$ in the semi-infinite half-space 59

Figure 4.15 A solid circular cylinder containing a penny-shaped crack 62

Figure 4.16 Finite element model of the cracked solid cylinder with the $J_{rg}(t)$-integral contours as illustrated 64

Figures 4.17a 4.17b Illustration of the path independence of the $J_{rg}(t)$-integral computation of $\bar{K}_I(t)$ for the cracked solid cylinder 65

Figure 4.18 Variation of $\bar{K}_I(t)$ with non-dimensionalized time for the cracked solid cylinder 67

Figure 4.19 Maximum values of $\bar{K}_I(t)$ for non-dimensionalized times, $c_1 t/L$, < 2.0 , for the cracked solid cylinder 70

PAGE

Figure 4.20	A thick-walled circular cylinder with an inner-circumferential edge crack	72
Figure 4.21	Finite element model of the cracked thick-walled cylinder used in the $J_{rg}(t)$-integral computations, with contours as illustrated .	73
Figure 4.22a	Finite element model of the cracked thick-walled cylinder used in the linear extrapolation technique, excluding crack-tip details	75
Figure 4.22b	Crack-tip details of the finite element model of the thick-walled cylinder used in the linear extrapolation technique	76
Figures 4.23a 4.23b	Illustration of the path independence of the $J_{rg}(t)$-integral computation of $\bar{K}_I(t)$ for the cracked thick-walled cylinder	78
Figure 4.24	Illustration of obtaining $\bar{K}_I(t)$ by using the linear extrapolation technique	79
Figure 4.25	Variation of $\bar{K}_I(t)$ with non-dimensionalized time for the cracked thick-walled cylinder	81
Figure 4.26	Maximum values of $\bar{K}_I(t)$ for the cracked thick-walled cylinder	83

NOMENCLATURE

a	radius of the crack tip
A	area enclosed by the contours Γ, Γ_p, and Γ_s
A^+	area A at $\theta = +\alpha/2$
A^-	area A at $\theta = -\alpha/2$
$[B]$	finite element strain-displacement matrix
c_1	$= \sqrt{\frac{\lambda+2\mu}{\rho}}$, dilatational wave speed
c_2	$= \sqrt{\frac{\mu}{\rho}}$, shear wave speed
$[C]$	finite element elasticity matrix
E	Young's modulus
$\mathbf{f}$	vector of body forces per unit mass
$\{F^e\},\{F\}$	element and global nodal-force vectors, respectively
$\{\Delta\tilde{F}_t\}$	effective global nodal-force-increment vector
$\mathbf{g}$	vector of external surface tractions
$H(t)$	unit Heaviside step function
I_1, I_2	integrals given by equations (2.24)
J	path-independent J-integral by Rice [26]
$J_{rg}(t)$	path-independent energy-flux integral for stationary cracks under general axisymmetric mode I conditions

K_{I_s}	static mode I (opening mode) stress intensity factor
K_d	a critical value of $K(t)$ occurring at the onset of crack propagation, is a material property
$K(t)$	dynamic stress intensity factor
$K_I(t)$	dynamic mode I stress intensity factor
$\bar{K}_I(t)$	normalized dynamic mode I stress intensity factor
$\bar{K}_{I_{max}}$	maximum value over time of the normalized dynamic mode I stress intensity factor
$K_I'(R,t)$	variable used in the linear extrapolation technique which tends to $K_I(t)$ as $R \rightarrow 0$
$\bar{K}_I'(R,t)$	normalized form of $K_I'(R,t)$
$[K^e]$,$[K]$	element and global stiffness matrices, respectively
$[\tilde{K}]$	effective global stiffness matrix
L	a characteristic length for a structure
Δl	a characteristic dimension of a finite element
Lt	in the limit
$[M^e]$,$[M]$	element and global mass matrices, respectively
n	outward unit surface-normal vector
$[N]$	finite element displacement-interpolation matrix
$\mathbf{O}(h)$	of the order of the quantity h
$P(t)$	time varying applied pressure
P_o	time-invariant applied pressure
Q	function describing the rate of work done in the solid volume V

r	global radial cylindrical coordinate
R	local radial polar coordinate originating at the crack tip
S	surface partially enclosing the volume V
S_s	surface of the crack faces
S_p	surface surrounding the fracture-process region
S^e	surface of a finite element
t	time
T	kinetic energy
$\mathbf{T}_n$	stress vector defined with respect to the vector $\mathbf{n}$
$\mathbf{u}$	displacement vector
$\{\Delta u_t\}$	nodal displacement-increment vector
U	potential energy
V	control volume over which the $J_{rg}(t)$-integral is evaluated
V^e	volume of a finite element
W	$= \int_0^{\varepsilon^e_{ij}} \sigma_{ij} d\varepsilon^e_{ij}$, elastic strain energy density function
x	global cartesian coordinate
X_1, X_2	local moving cartesian coordinates originating at the crack tip
y	global cartesian coordinate

z	global cylindrical coordinate
α	angle subtended by the control volume V
β	Newmark β integration parameter
γ	Newmark β integration parameter
Γ	portion of the $J_{rg}(t)$-integral contour not on the crack surfaces
$\Gamma_1, \Gamma_2, \ldots$	specific forms of Γ
Γ_s	portion of the $J_{rg}(t)$-integral contour on the crack surfaces
Γ_p	contour surrounding the fracture-process region in the r-z plane
δ_{ij}	= 1 for i=j = 0 for $i \neq j$, Kronecker delta
ε	infinitesimal strain tensor
$\varepsilon_{\theta\theta}$	hoop strain
ε^e_{ij}	elastic strain tensor
ε^*_{ij}	inelastic strain tensor
η	specific values of non-dimensionalized time, $c_1 t/L$
θ	global angular cylindrical coordinate
λ	Lame's constant
μ	shear modulus
ν	Poisson's ratio
π	3.1415926
ρ	material mass density

$\boldsymbol{\sigma}$	stress tensor
σ_{rr}	radial-stress component in the cylindrical coordinate system
$\sigma_{\theta\theta}$	hoop-stress component in the cylindrical coordinate system
σ_{zz}	axial-stress component in the cylindrical coordinate system
σ_{rz}	rz-component of shear stress in the cylindrical coordinate system
σ_{xx}	x-component of normal stress in the cartesian coordinate system
σ_{yy}	y-component of normal stress in the cartesian coordinate system
σ_{xy}	xy-component of shear stress in the cartesian coordinate system
$\sigma(t)$	time varying applied tensile stress
σ_o	time-invariant applied tensile stress
τ_{max}	maximum shear stress
ϕ	local angular polar coordinate at the crack tip
Φ	functional which is the time average of the difference between the kinetic and potential energies of a body
ψ	angle between $\mathbf{n}$ and the r-coordinate
∞	infinity

prefix δ	denotes a first-order virtual quantity
prefix Δ	denotes a finite increment
subscripts i or j for the cylindrical coordinate system	i or j = 1,2,3 corresponds to the r,θ,z components, respectively
subscript $\vert_{inner}$	applicable to an inner-edge crack
subscript $\vert_{outer}$	applicable to an outer-edge crack
superscript ^{T}	transpose
$\cdot$	scalar product
∇	gradient
div	divergence
$tr = \delta_{ij}(\ )_{ij}$	trace of tensor
dot superscript	derivative with respect to time, t
$\rightarrow$	approaches
[ ]	rectangular matrix
{ }	column vector

CHAPTER ONE

INTRODUCTION

The analysis of the response of cracked solids to dynamic loads is essential in predicting the stability of flawed structures subjected to such conditions. If the time required for the magnitude of the applied load to reach its maximum value is less than one-half the dominant period of the structure, then the effects from material inertia should be considered [1]. By limiting the material behaviour to be elastic, the methodology of elastodynamic fracture mechanics can be applied. To date, the vast majority of research in this field has been concerned with cracks under planar conditions.† However, practical situations may arise for which the assumption of axisymmetric conditions would be more appropriate in obtaining an approximate solution, or a bound on the solution, as has been put forth in static†† analyses [2-8]. A typical example would be a thick-walled pipe with a partially-through inner-edge crack around a portion of its circumference, subjected to a shock loading. The lack of solutions to such problems motivated the author to develop a technique for the investigation of axisymmetric stationary-crack problems under dynamic loading conditions.

---

† In this thesis "conditions" shall imply geometry and loading.

†† In this thesis the term "static" shall refer to cases in which material inertia effects are neglected.

1.1 Review of Elastodynamic Analyses of Stationary Cracks

The major efforts in elastodynamic fracture mechanics have been focused on determining the time-dependent dynamic stress intensity factor, $K(t)$. Like its static counterpart, $K(t)$ is a crack-tip parameter and represents the magnitude of the stress field near a crack tip [1]. It is assumed that at the onset of crack propagation $K(t)$ reaches a critical value, K_d, which is a material property and is independent of the rate of loading [9]. Thus, it can be estimated whether crack propagation will occur in a flawed structure by comparing the peak value of $K(t)$ to the experimentally determined K_d.

Closed-form solutions for the dynamic stress intensity factor of stationary cracks are limited to simple problems under planar [1,10-12] and axisymmetric [1,11,13] conditions. Alternatively, approximate techniques used in conjunction with the finite difference [14] and finite element [15-24] methods have been applied with success to planar problems. In these techniques the finite element approach appears to be more suitable.

A simple procedure was utilized by Chen and Wilkins [14] and by Kobayashi *et al.* [15], whereby $K(t)$ was calculated by matching the numerically computed near-tip

stress field to an analytical solution, which is in a generalized form as a function of $K(t)$. By considering the crack illustrated in Figure 1.1 to be under mode I (the opening mode)† loading conditions, this stress field is given by [1]

$$\sigma_{ij}(t) = \frac{K_I(t)}{\sqrt{2\pi R}} F_{ij}(\phi) + \mathbf{0}(1) \quad . \tag{1.1}$$

In the above equation $\sigma_{ij}(t)$ is the time-dependent stress tensor, t is time, $K_I(t)$ is the time-dependent mode I dynamic stress intensity factor, R is the radius from the crack tip, ϕ is the polar angle about the crack tip and $F_{ij}(\phi)$ is a dimensionless function of ϕ . In equation (1.1) the dependence on geometry and loading arises through $K_I(t)$. However, due to the crack-tip stress singularity this method requires a very fine mesh in the near-tip region, resulting in a large number of required degrees of freedom and an unavoidable error in the numerical time-integration of the equations of motion [18].

Special singular finite elements, located at the crack tip, which embody the analytical near-tip displacement field in the element shape functions, have been employed by Aberson et al. [17] and others [18-21]. These elements

---

† A description of the three modes of fracture is presented in reference [25].

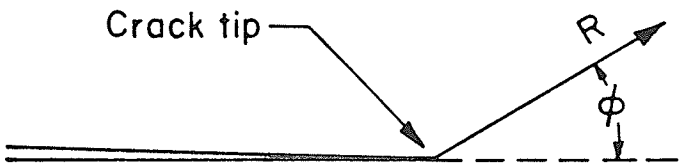

Figure 1.1 - A coordinate system at the crack tip.

may be used in conjunction with a relatively coarse mesh, and some include $K(t)$ as a degree of freedom. However, singular elements generally require a major programming effort and the ability of these special shape functions to model wave propagation has been criticized [18].

Alternatively, Bažant *et al.* [18], Glazik, Jr. [21] and Mall [22] (as discussed in reference [23]) employed a structural calibration technique. Their procedure was to determine, for a given mesh, the ratio between $K(t)$ and a near-tip nodal displacement for some simple loading and to assume this ratio to be constant for all loads. However, the method is limited to those cases for which $K(t)$ can be determined in advance for some simple loading condition.

An energy approach has been followed by extending the concept of the path-independent J-integral by Rice [26] to elastodynamic crack analyses [23,24,31-34]. Such path-independent integrals yield a value for $K(t)$ computed truly at the crack tip. These integrals may be evaluated in conjunction with a conventional numerical dynamic code. As well, the adverse effect of the theoretical crack-tip singularity on the numerical accuracy is only minor and relatively coarse meshes may be used. Kishimoto *et al.* [24] have produced results superior to those obtained from singular elements where equivalent grids were used for both methods. These various path-independent integrals will be discussed in Chapter Two.

1.2 Scope of Thesis

From the above review it appears that the path-independent energy integral is a promising technique for the approximate computation of $K(t)$. Such a path-independent integral is derived for stationary cracks under axisymmetric mode I conditions in Chapter Two in a generalized form, including material inertia effects. The integral is reduced to a form suitable for elastodynamic analysis and is related to $K(t)$. To evaluate this integral numerically, a conventional static (analysis) finite element computer program was extended to a version capable of modelling wave propagation in linear elastic solids, following the formulations presented in Chapter Three. After testing the dynamic code by using three cases, the elastodynamic version of the integral was implemented into the code. Two problems involving axisymmetric cracks subjected to dynamic loading were analysed to obtain the time history of $K(t)$. The results were compared to other solutions. The five numerical studies are presented in Chapter Four. Conclusions drawn from the present work and recommendations for future development are expressed in Chapter Five.

CHAPTER TWO
A GENERAL PATH-INDEPENDENT ENERGY-FLUX INTEGRAL FOR STATIONARY CRACKS UNDER AXISYMMETRIC MODE I CONDITIONS

2.1 Introduction

Determining the energy flux into the tip of an extending† crack is a well-established technique for the approximate analysis of flaws [23,26-34]. In this context the energy flux is defined as the flow of energy to the crack tip with respect to a change in the surface area of a crack face [27]. This energy flux is thus a true crack-tip parameter and is consistent with the physical mechanism of the irreversible energy flux required to extend a crack. The energy flux to the crack tip is formulated from a structural-energy balance and is expressed in the form of a path-independent integral which does not require an accurate description of crack-tip conditions. To analyse practical problems, these integrals must be evaluated from the numerical solution of the appropriate fracture problem.

In this chapter a general path-independent energy-flux integral will be derived specifically for axisymmetric crack problems. The technique presented by Kishimoto et al.

---

† The crack may be assumed to extend by an infinitesimal amount only.

[34] in the cartesian coordinate system shall be followed in the cylindrical coordinate system, due to their straightforward approach and yet generality of the result. The integral so derived is based on stationary cracks under mode I conditions only and will include the effects of material inertia, body forces and thermal, plastic strains. The elastodynamic version of this integral will then be related to the dynamic stress intensity factor.

2.2 Review of Path-Independent Energy-Flux Integrals

The first path-independent energy-flux integral was the J contour integral proposed by Rice [26,27] for two-dimensional planar static crack problems in elastic solids.† Rice defined J to be the flux of strain energy to the crack tip with respect to crack-face extension and he expressed J in terms of the stress intensity factor under the restriction of linear elastic material behaviour. The J-integral concept has been extended to the elastodynamic analysis of planar crack problems. Such integrals represent the flux of strain and kinetic energies to the crack tip and are generally employed to determine the dynamic stress intensity factor. A contour integral

---

† The major application of the J-integral has been towards analysing static crack problems with the presence of small or large scale plasticity.

based on viscoelastic material behaviour has been derived by Nilsson [31] who formulated the problem in the Laplace transform domain rather than the time domain. The related dynamic stress intensity factor is expressed in the Laplace transform domain and a numerical inversion is required to obtain $K(t)$ in the time domain. Gurtin [32] has proposed a contour integral based on an energy conservation law but the integrand is presented in a time-convoluted form. The J-integral of Rice has been extended by Bui [33] (as discussed by Mall [23]) through the addition of inertia terms with the inclusion of an area integral to achieve path independence. Mall [23] has simplified Bui's expression to the form of an inertia-force area integral added to J and verifies his results. A generalized integral for two- or three-dimensional crack problems has been developed by Kishimoto et al. [34] which accounts for material inertia, body forces and thermal, plastic strains. Their expression is based on the rate of work done by these various mechanisms and will reduce to Mall's integral in the two-dimensional elastodynamic case.

A logical means of obtaining a path-independent energy-flux integral capable of analysing axisymmetric elastodynamic crack problems would be to reduce the cartesian-

coordinate based three-dimensional integral of Kishimoto et al., $\hat{J}_{3D}$, to an axisymmetric form. A similar procedure was adopted by Bergkvist and Huong [5,7] and independently by Astiz et al. [6], in the static case. However, $\hat{J}_{3D}$ does not include the dependence of the increment in crack-face surface area on the instantaneous crack radius and, furthermore, the boundaries of integration are planar. For these reasons $\hat{J}_{3D}$ is incompatible with an axisymmetric analysis.

2.3 Physical Model

Consider the straight-line-crack configuration illustrated in Figure 2.1. The fixed (r,z) and moving (X_1,X_2) coordinate systems lie in the same plane such that the origin of (X_1,X_2) is always located at the tip of the crack (as depicted by the movement from 0 to 0' during crack extension). As discussed by Broberg [29], it is assumed that a fracture-process region surrounds the crack tip. The mechanisms of void growth and coalescence occur in this region and, thus, the material does not behave as a continuum. The fracture-process region is defined to be the smallest region encompassing the crack tip such that all the material outside the region's boundary still obeys the laws of continuum mechanics. The shape of the region is assumed to be similar to the fracture cohesive zone proposed by Barenblatt [35]†. Consequently, the region moves with

† As presented in reference [27].

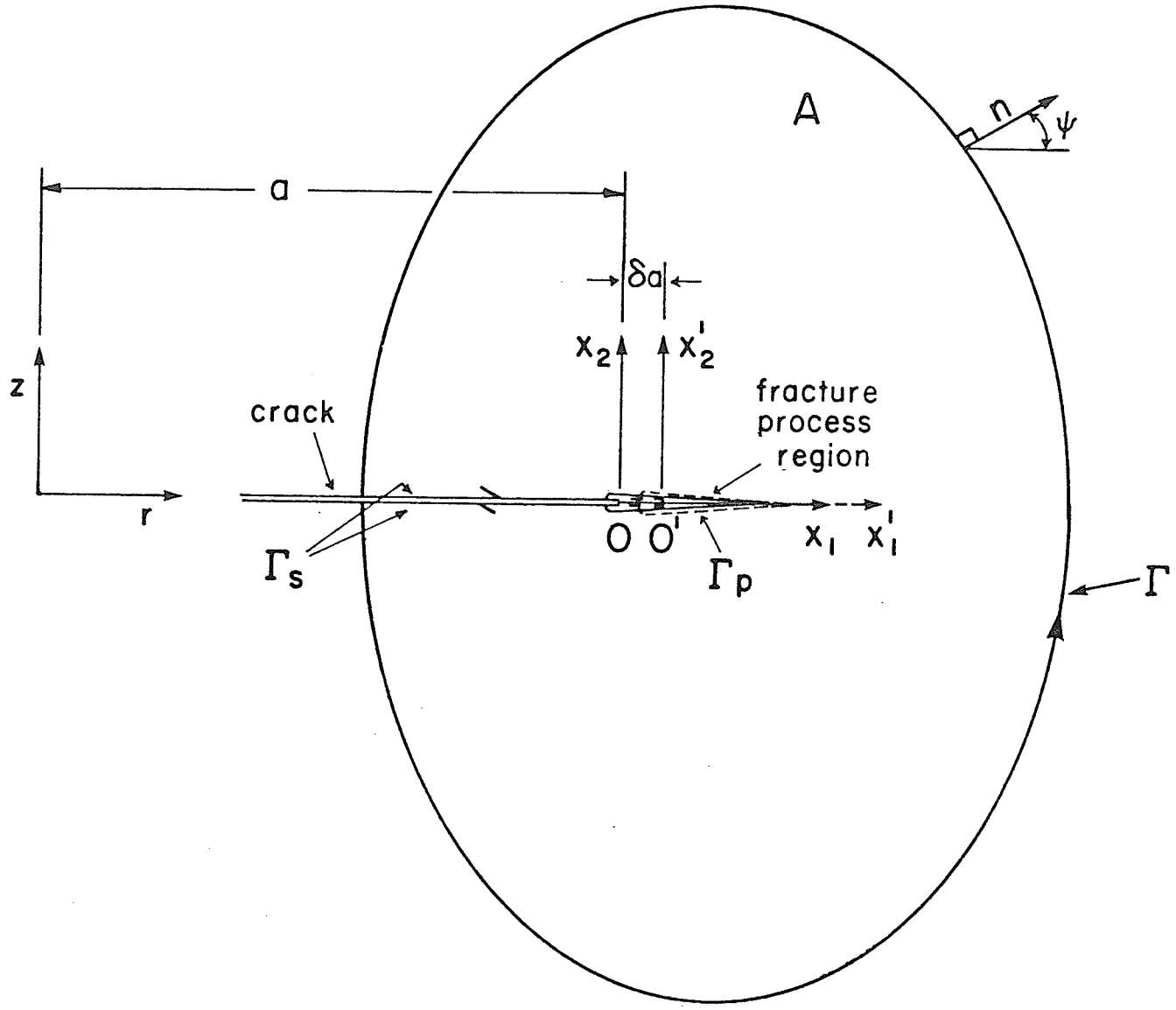

Figure 2.1 - Line-crack configuration.

the crack tip, as indicated by the dashed lines. Let the counterclockwise contour Γ_p surround the area of the fracture-process region and let the counterclockwise contour Γ be arbitrary apart from meeting the upper and lower crack faces at the same position along the crack length. The contour Γ_s runs along the crack faces in the directions shown, joining Γ to Γ_p, and the area A is enclosed by a closed loop composed of the contours Γ_p, Γ and Γ_s. The direction of the outward unit surface-normal vector,† $\mathbf{n}$, relative to the r-axis, is specified by the angle ψ.

Consider, also, the axisymmetric cylinder segment containing an axisymmetric line crack, in a fixed (r,θ,z) cylindrical coordinate system as illustrated in Figure 2.2. The segment represents a section of a solid or hollow circular cylinder, centred about the (r,θ,z) origin, containing an axisymmetric crack of tip radius a lying in the r-θ plane. The cylinder is "sliced" through the r-z planes at $\theta = \pm\alpha/2$ to form the segment whose shape in the r-z plane (depicted as rectangular) is arbitrary. Let Figure 2.1 be a sectional view in the r-z plane of the control volume in the cylinder segment, which also subtends the angle $-\alpha/2 \leq \theta \leq +\alpha/2$. For illustrative simplicity, Γ is depicted as rectangular in shape, Γ_p as elliptical,

† A symbol in bold type shall generally denote the coordinate-invariant form of a vector or a second-order tensor.

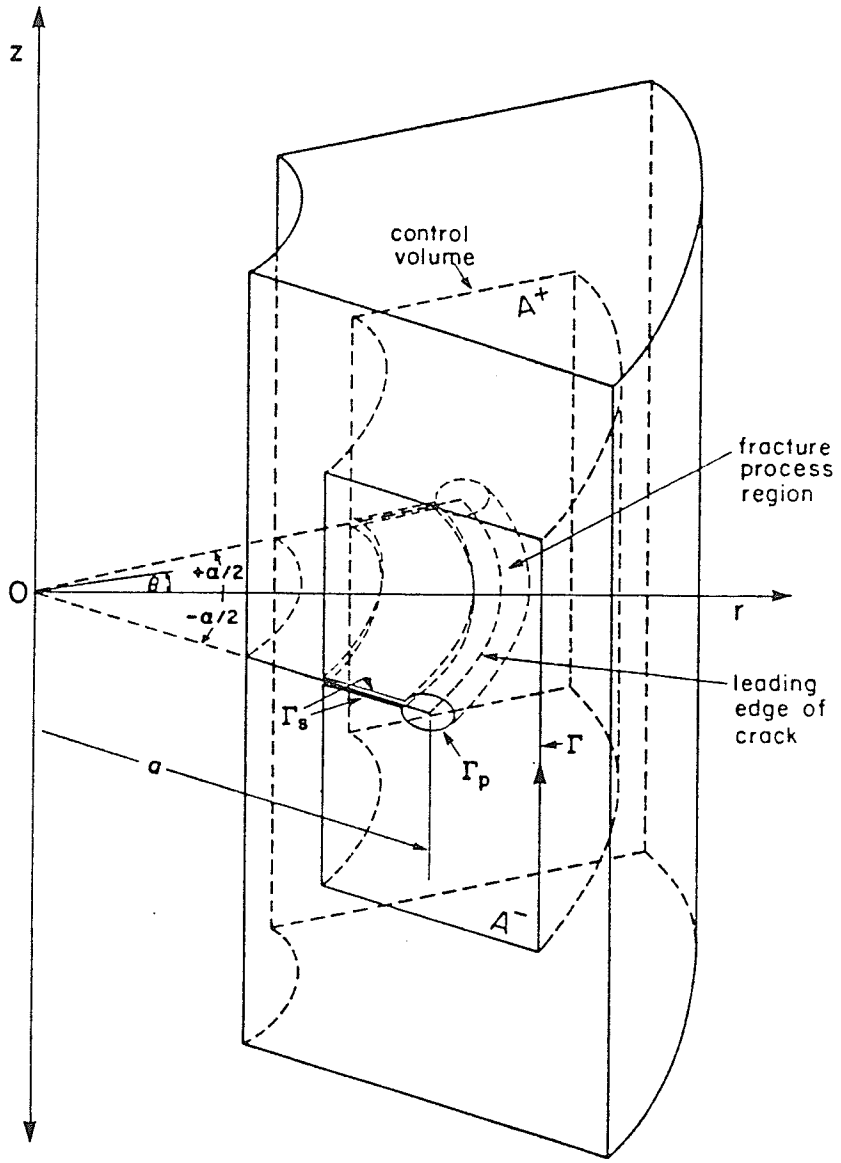

Figure 2.2 - Cracked-cylinder segment containing a control volume.

and other crack-tip details have been omitted. The areas A^+ and A^- lie in the r-z planes at $\theta = +\alpha/2$ and $-\alpha/2$, respectively. With reference to Figure 2.3, the surfaces S, S_s and S_p are formed by rotating the contours Γ, Γ_s and Γ_p, respectively, through the angle α. As well, the control volume V is created upon rotating the area A through the angle α, and is totally enclosed by the surfaces S, S_s, S_p, A^+ and A^-. The surface S comprises the upper, lower, concave and convex surfaces of V; S_s are the crack faces and S_p is the surface at the boundary of the fracture-process region. The material in the control volume shall be restricted to be homogeneous.

A similar physical model is applicable to cylinders with outer-edge cracks. This may be envisioned from Figure 2.2 by relocating the origin of the (r,θ,z) coordinate system (always located at the centre of the cylinder) to the right-hand side of the cylinder segment. The concave portion of S is then on the right-hand side of the segment whilst the convex portion of S is on the left-hand side. In such cases X_1 and r act in opposite directions and the crack-tip radius a will decrease rather than increase with crack extension.

2.4 Energy Flux into the Fracture-Process Region

The energy flux into the tip of a crack may be modelled realistically as the energy flux into the fracture-process region [29], assumed to be equal to the

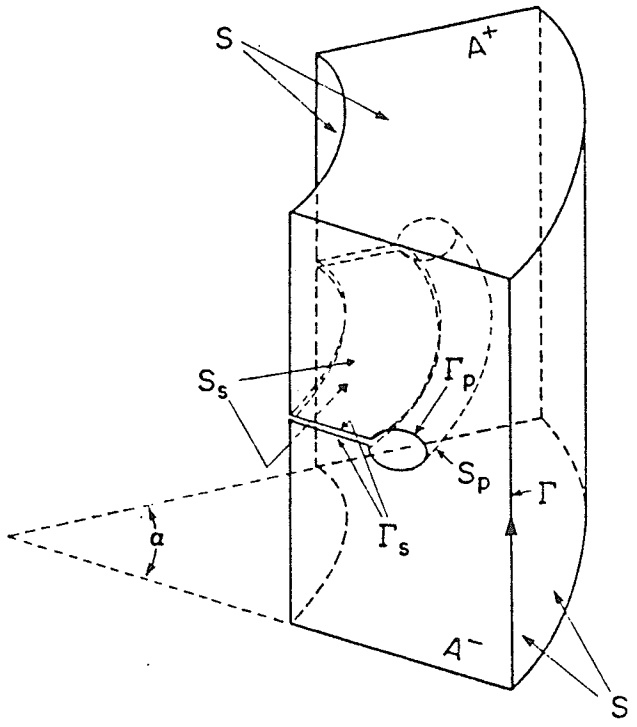

Figure 2.3 - Illustration of the surface enclosing the control volume.

flux of work done by the stress vector on the boundary of the region [34]. To evaluate this work flux for an inner-edge crack, consider the virtual crack extension, δa, as depicted in Figure 2.1, and the corresponding virtual displacements, $\delta \mathbf{u}$. The work flux is equal to the virtual work (per unit area) done by the stress vector,† $\mathbf{T}_n$, in a virtual displacement of $\delta \mathbf{u}$, divided by the virtual crack-surface extension of one face, $\alpha a \delta a$. Thus, by denoting $J_{rg}(t)$ to be the time-dependent energy flux into the crack tip and by neglecting second-order virtual quantities, one may write with reference to Figures 2.2 and 2.3,

$$J_{rg}(t)\Big|_{inner} = \frac{1}{\alpha a} \int_{S_p} \mathbf{T}_n \cdot \frac{\delta \mathbf{u}}{\delta a} \, dS \quad , \tag{2.1}$$

where it is assumed that the energy flux across the ends of the fracture-process region (at $\theta = +\alpha/2, -\alpha/2$) is zero.

The displacements on S_p are a function of the (X_1, X_2) coordinate system and, in the limit, $\delta \mathbf{u}/\delta a$ can be expressed as

$$\underset{\delta a,\, \delta \mathbf{u} \longrightarrow 0}{\text{Lt}} \frac{\delta \mathbf{u}}{\delta a} = \frac{\partial \mathbf{u}}{\partial a} + \frac{\partial \mathbf{u}}{\partial X_1} \frac{\partial X_1}{\partial a} + \frac{\partial \mathbf{u}}{\partial X_2} \frac{\partial X_2}{\partial a} \quad . \tag{2.2}$$

The relation between the (r,θ,z) and (X_1, X_2) coordinate systems is given by

$$X_1 = r - a$$

and

$$X_2 = z \tag{2.3}$$

---

† $\mathbf{T}_n$ shall always be defined with respect to the outward unit surface-normal vector, $\mathbf{n}$.

from which equation (2.2) reduces to

$$\lim_{\delta a,\ \delta \mathbf{u} \to 0} \frac{\delta \mathbf{u}}{\delta a} = \frac{\partial \mathbf{u}}{\partial a} - \frac{\partial \mathbf{u}}{\partial X_1} \quad . \tag{2.4}$$

The partial derivative $\partial \mathbf{u}/\partial r$ may be expanded using the chain rule as

$$\frac{\partial \mathbf{u}}{\partial r} = \frac{\partial \mathbf{u}}{\partial X_1} \frac{\partial X_1}{\partial r} + \frac{\partial \mathbf{u}}{\partial X_2} \frac{\partial X_2}{\partial r}$$

and, from equations (2.3),

$$\frac{\partial \mathbf{u}}{\partial r} = \frac{\partial \mathbf{u}}{\partial X_1} \quad . \tag{2.5}$$

By substituting equation (2.5) into (2.4) one may write equation (2.1) as

$$J_{rg}(t)\Big|_{inner} = \frac{1}{\alpha a} \int_{S_p} \mathbf{T}_n \cdot \left(\frac{\partial \mathbf{u}}{\partial a} - \frac{\partial \mathbf{u}}{\partial r}\right) dS \quad . \tag{2.6}$$

It is assumed that the characteristic dimension of the fracture-process region is much less than the crack length, such that the mechanisms occurring in and on the boundary of the region are autonomous with respect to geometry and loading [29]. Under this assumption $\partial \mathbf{u}/\partial a = 0$ on S_p and equation (2.6) can be written as a rate of work done with respect to the r-coordinate only,

$$J_{rg}(t)\Big|_{inner} = -\frac{1}{\alpha a} \int_{S_p} \mathbf{T}_n \cdot \frac{\partial \mathbf{u}}{\partial r} dS \quad . \tag{2.7a}$$

A similar formulation can be followed for a cylinder with an outer-edge crack. A virtual extension of an outer-edge crack will result in a virtual change $-\delta a$ in the crack-tip radius a. Thus, in this case equation (2.1) will possess an opposite sign;

$$J_{rg}(t)\Big|_{outer} = -\frac{1}{\alpha a}\int_{S_p} \mathbf{T}_n \cdot \frac{\delta \mathbf{u}}{\delta a}\, dS \quad .$$

As well, for an outer-edge crack $X_1 = a - r$, and equation (2.4) becomes

$$\underset{\delta a,\ \delta \mathbf{u} \longrightarrow 0}{Lt} \frac{\delta \mathbf{u}}{\delta a} = \frac{\partial \mathbf{u}}{\partial a} + \frac{\partial \mathbf{u}}{\partial X_1} \quad ,$$

and equation (2.5) is written as

$$\frac{\partial \mathbf{u}}{\partial r} = -\frac{\partial \mathbf{u}}{\partial X_1} \quad .$$

Upon performing the appropriate substitutions, equation (2.7) is, for an outer-edge crack,

$$J_{rg}(t)\Big|_{outer} = \frac{1}{\alpha a}\int_{S_p} \mathbf{T}_n \cdot \frac{\partial \mathbf{u}}{\partial r}\, dS \quad . \qquad (2.7b)$$

2.5 Energy Flux Expressed as a Path-Independent Integral

The concept of $J_{rg}(t)$ as the energy flux into the fracture-process region enables one to perform an energy balance on the control volume V and the surrounding surfaces (for inner- or outer-edge cracks) with the result (see Figure 2.3)

$J_{rg}(t)$ = flux of work performed by tractions $\mathbf{T}_n$ on the bounding surfaces $S + S_s + A^+ + A^-$ - rate of work done in V . (2.8)

The fluxes or rates are with respect to the crack-surface extension. However, equations (2.7) demonstrate that $J_{rg}(t)$ may be conveniently represented in terms of an energy rate with respect to r . Upon doing so, to retain a consistent energy balance the right-hand side of equation (2.8) must also be expressed in terms of energy rates with respect to r ;

$$J_{rg}(t)\Big|_{\substack{\text{inner}\\\text{outer}}} = \frac{1}{\alpha a}\left(\mp \int_{S + S_s + A^+ + A^-} \mathbf{T}_n \cdot \frac{\partial \mathbf{u}}{\partial r}\, dS - Q\right) . \tag{2.9}$$

In this expression Q is the rate of work done with respect to r in V and from equation (2.7) the negative and positive signs of the first term correspond to inner- and outer-edge cracks, respectively. Equation (2.9) is the desired path-independent expression for $J_{rg}(t)$, provided an explicit function for Q is found.

To obtain Q , first substitute equation (2.7) into (2.9) and replace $\mathbf{T}_n$ on S_p with its equal but opposite-signed counterpart defined with respect to the surface S_p of V . Upon rearranging,

$$Q\Big|_{\substack{\text{inner}\\\text{outer}}} = \mp \int_{S + S_s + S_p + A^+ + A^-} \mathbf{T}_n \cdot \frac{\partial \mathbf{u}}{\partial r}\, dS . \tag{2.10}$$

The stress tensor, $\boldsymbol{\sigma}$, is symmetric and is defined by the transformation [36];

$$\mathbf{T}_n = \boldsymbol{\sigma}\mathbf{n} \quad . \tag{2.11}$$

By substituting equation (2.11) into (2.10) and by employing the definition of the transpose of a tensor [36], one may write

$$Q_{\substack{\text{inner}\\\text{outer}}} = \mp \int_{S + S_s + S_p + A^+ + A^-} \mathbf{n} \cdot (\boldsymbol{\sigma}\frac{\partial \mathbf{u}}{\partial r}) \, dS \quad . \tag{2.12}$$

Gauss's divergence theorem [36] may be applied to equation (2.12) to obtain the desired volume integral for Q ;

$$Q_{\substack{\text{inner}\\\text{outer}}} = \mp \int_V \operatorname{div}(\boldsymbol{\sigma}\frac{\partial \mathbf{u}}{\partial r}) \, dV \quad . \tag{2.13}$$

By employing the definition of the divergence of a tensor field [36], equation (2.13) can be expressed as

$$Q_{\substack{\text{inner}\\\text{outer}}} = \mp \int_V \left(\operatorname{div}\boldsymbol{\sigma} \cdot \frac{\partial \mathbf{u}}{\partial r} + \operatorname{tr}\left(\boldsymbol{\sigma}^T (\nabla \frac{\partial \mathbf{u}}{\partial r})\right) \right) dV \quad , \tag{2.14}$$

where tr denotes the trace of a tensor.

To express Q in a form suitable for numerical computation, consider first the equations of motion [36],

$$\operatorname{div}\boldsymbol{\sigma} + \rho\mathbf{f} = \rho\ddot{\mathbf{u}} \quad , \tag{2.15}$$

where ρ is the homogeneous material's mass density, $\mathbf{f}$ is a vector of body forces per unit mass and an overhead dot denotes differentiation with respect to time. From equation (2.15) one may write the first term in the integrand of (2.14) as

$$\mathrm{div}\boldsymbol{\sigma} \cdot \frac{\partial \mathbf{u}}{\partial r} = \rho(\ddot{u}_i - f_i) \frac{\partial u_i}{\partial r} \quad , \tag{2.16}$$

where the right-hand side of equation (2.16) has been expressed in terms of components in the cylindrical coordinate system, such that $i = 1,2,3$ corresponds to the r,θ,z components, respectively.

The second term in the integrand of equation (2.14) may be expressed in component form as

$$\begin{aligned} \mathrm{tr}\left(\boldsymbol{\sigma}^T(\nabla\frac{\partial \mathbf{u}}{\partial r})\right) &= \delta_{ij}\, \sigma_{mi} (\nabla\frac{\partial \mathbf{u}}{\partial r})_{mj} \\ &= \sigma_{ij} (\nabla\frac{\partial \mathbf{u}}{\partial r})_{ij} \quad . \end{aligned} \tag{2.17}$$

It is shown in Appendix I that in the axisymmetric case,

$$\sigma_{ij} (\nabla\frac{\partial \mathbf{u}}{\partial r})_{ij} = \sigma_{ij} \frac{\partial \epsilon_{ij}}{\partial r} + \frac{\sigma_{\theta\theta}\epsilon_{\theta\theta}}{r} \tag{2.18}$$

where ϵ_{ij} is the infinitesimal strain tensor. Upon comparing equations (2.17) and (2.18) one may write

$$\mathrm{tr}\left(\boldsymbol{\sigma}^{T}\left(\nabla\frac{\partial \mathbf{u}}{\partial r}\right)\right) = \sigma_{ij}\,\frac{\partial \varepsilon_{ij}}{\partial r} + \frac{\sigma_{\theta\theta}\varepsilon_{\theta\theta}}{r} \quad . \tag{2.19}$$

Following reference [34] the strain tensor is decomposed into the sum of the elastic and inelastic strain tensors. The elastic strain tensor, ε^{e}_{ij}, is assumed to, alone, uniquely define the stress state. The inelastic (thermal, plastic) strain tensor,† ε^{*}_{ij}, is assumed to not explicitly contribute to the stress state. Thus, by letting

$$\varepsilon_{ij} = \varepsilon^{e}_{ij} + \varepsilon^{*}_{ij} \quad , \tag{2.20}$$

one may expand equation (2.19) to

$$\mathrm{tr}\left(\boldsymbol{\sigma}^{T}\left(\nabla\frac{\partial \mathbf{u}}{\partial r}\right)\right) = \sigma_{ij}\,\frac{\partial \varepsilon^{e}_{ij}}{\partial r} + \sigma_{ij}\,\frac{\partial \varepsilon^{*}_{ij}}{\partial r} + \frac{\sigma_{\theta\theta}\varepsilon_{\theta\theta}}{r} \quad . \tag{2.21}$$

The elastic strain energy density function, W, is an explicit function of the elastic strains only [37], and it is demonstrated in Appendix II that

---

† In the analysis σ_{ij} and ε_{kl} are known and if, for example, the material's elastic behaviour is linear, then ε^{*}_{kl} can be determined by inverting the relation [43]

$$\sigma_{ij} = C_{ijkl}(\varepsilon_{kl} - \varepsilon^{*}_{kl}) \quad ,$$

where C_{ijkl} is the elasticity tensor.

$$\sigma_{ij} \frac{\partial \varepsilon^{e}_{ij}}{\partial r} = \frac{\partial W}{\partial r} \quad . \tag{2.22}$$

Upon substituting equation (2.22) into (2.21), and subsequently (2.16) and (2.21) into (2.14), a more tractable expression for Q is obtained as

$$Q_{\left|\substack{\text{inner}\\\text{outer}}\right.} = \mp \int_V \left(\rho (\ddot{u}_i - f_i) \frac{\partial u_i}{\partial r} + \frac{\partial W}{\partial r} + \frac{\sigma_{\theta\theta} \varepsilon_{\theta\theta}}{r} + \sigma_{ij} \frac{\partial \varepsilon^{*}_{ij}}{\partial r} \right) dV \quad . \tag{2.23}$$

The terms in this last equation represent the rates of work done by the material's inertia forces, body forces and the stress tensor due to elastic and inelastic strains, respectively. This result is consistent with the definition of Q as the rate of work done in the control volume, V .

By substituting equation (2.23) for Q into (2.9) one obtains a path-independent relation for $J_{rg}(t)$;

$$J_{rg}(t)_{\left|\substack{\text{inner}\\\text{outer}}\right.} = \pm \frac{1}{\alpha a} \int_V \left(\rho(\ddot{u}_i - f_i) \frac{\partial u_i}{\partial r} + \frac{\partial W}{\partial r} + \frac{\sigma_{\theta\theta} \varepsilon_{\theta\theta}}{r} + \sigma_{ij} \frac{\partial \varepsilon^{*}_{ij}}{\partial r} \right) dV$$

$$\mp \frac{1}{\alpha a} \int_{S + S_s + A^{+} + A^{-}} T_{n_i} \frac{\partial u_i}{\partial r} \, dS \quad . \tag{2.24a}$$

Or, for brevity,

$$J_{rg}(t)_{\left|\substack{\text{inner}\\\text{outer}}\right.} = \pm I_1 \mp I_2 \quad . \tag{2.24b}$$

2.6 Reduction of Surface and Volume Integrals

It is possible to simplify the integration of equation (2.24) by taking advantage of the invariance of quantities with respect to the θ-coordinate. By performing the substitution

$$dV = \alpha r dA \quad ,$$

where dA is an infinitesimal element of area A, one may convert the volume integral, I_1, to an integral evaluated over the area A,

$$I_1 = \int_A \left(\left(\rho (\ddot{u}_i - f_i) \frac{\partial u_i}{\partial r} + \sigma_{ij} \frac{\partial \overset{*}{\varepsilon}_{ij}}{\partial r} \right) \frac{r}{a} + \frac{\sigma_{\theta\theta} \varepsilon_{\theta\theta}}{a} \right) dA + \int_A \frac{\partial W}{\partial r} \frac{r}{a} dA \quad . \tag{2.25}$$

By assuming the cross-sectional area of the fracture-process region in the r-z plane to be relatively small, the last term in equation (2.25) may be integrated by parts, as in Appendix III, to yield

$$\int_A \frac{\partial W}{\partial r} \frac{r}{a} dA = \int_\Gamma W \cos(\psi) \frac{r}{a} d\Gamma - \int_A \frac{W}{a} dA \quad .$$

Therefore,

$$I_1 = \int_\Gamma W \cos(\psi) \frac{r}{a} d\Gamma + \int_A \left(\left(\rho (\ddot{u}_i - f_i) \frac{\partial u_i}{\partial r} + \sigma_{ij} \frac{\partial \overset{*}{\varepsilon}_{ij}}{\partial r} \right) \frac{r}{a} + \frac{(\sigma_{\theta\theta} \varepsilon_{\theta\theta} - W)}{a} \right) dA \quad . \tag{2.26}$$

In focusing attention on I_2, refer to equation (2.11) and observe that for any particular position in the r-z plane, T_{n_i} on A^+ will be equal in magnitude and opposite in sign to T_{n_i} on A^-. Thus the integration on $A^+ + A^-$ will cancel leaving

$$I_2 = \frac{1}{\alpha a} \int_{S + S_s} T_{n_i} \frac{\partial u_i}{\partial r} \, dS \quad .$$

By using the relation

$$dS = \alpha r \, d\Gamma \quad ,$$

I_2 may be written as the contour integral

$$I_2 = \int_{\Gamma + \Gamma_s} T_{n_i} \frac{\partial u_i}{\partial r} \frac{r}{a} \, d\Gamma \quad . \tag{2.27}$$

A conventional numerical code computes the components of σ_{ij}, but not those of T_{n_i}. Therefore, the transformation given by equation (2.11) is substituted into (2.27) prior to performing the scalar product and, upon evaluating the scalar product (see Appendix IV for details),

$$I_2 = \int_{\Gamma} \left((\sigma_{rr} \frac{\partial u_r}{\partial r} + \sigma_{rz} \frac{\partial u_z}{\partial r}) \cos\psi + (\sigma_{rz} \frac{\partial u_r}{\partial r} + \sigma_{zz} \frac{\partial u_z}{\partial r}) \sin\psi \right) \frac{r}{a} \, d\Gamma$$

$$- \int_{\Gamma_s} P \frac{\partial u_z}{\partial r} \sin(\psi) \frac{r}{a} \, d\Gamma \quad , \tag{2.28}$$

where P is the pressure applied to the crack faces. An

expression for $J_{rg}(t)$ which is suitable for direct numerical computation can now be written by substituting equations (2.26) and (2.28) into (2.24). Consequently,

$$J_{rg}(t)\Big|_{\substack{\text{inner}\\\text{outer}}} = \pm \int_{\Gamma} \left((W - \sigma_{rr} \frac{\partial u_r}{\partial r} - \sigma_{rz} \frac{\partial u_z}{\partial r})\cos\psi - (\sigma_{rz} \frac{\partial u_r}{\partial r} + \sigma_{zz} \frac{\partial u_z}{\partial r})\sin\psi \right) \frac{r}{a} \, d\Gamma$$

$$\pm \int_{\Gamma_s} P \frac{\partial u_z}{\partial r} \sin(\psi) \frac{r}{a} \, d\Gamma$$

$$\pm \int_{A} \left(\left(\rho(\ddot{u}_i - f_i) \frac{\partial u_i}{\partial r} + \sigma_{ij} \frac{\partial \overset{*}{\varepsilon}_{ij}}{\partial r} \right) \frac{r}{a} + \frac{(\sigma_{\theta\theta} \overset{*}{\varepsilon}_{\theta\theta} - W)}{a} \right) dA \quad . \tag{2.29}$$

The positive and negative signs on the right-hand side of equation (2.29) correspond to inner- and outer-edge cracks, respectively.

2.7 Limiting Cases

By neglecting terms in equation (2.29) involving material inertia, body forces, inelastic strains and crack-surface pressure, $J_{rg}(t)\big|_{\text{inner}}$ reduces to the axisymmetric integral developed for such a situation by Bergkvist and Huong [5] and by Astiz [6]. As well, upon combining equations (2.26) and (2.27) it is observed that all terms in the planar mode I $\hat{J}_1$ integral by Kishimoto *et al.* [34] are included with a multiplier of r/a in $J_{rg}(t)\big|_{\text{inner}}$. This r/a factor arises from the cylinder-segment control volume used in formulating $J_{rg}(t)$ as opposed to the planar control volume for $\hat{J}_1$. In the limit, for a finite r,

$$\underset{a \to \infty}{\text{Lt}} \; J_{rg}(t)\big|_{\text{inner}} \to \hat{J}_1 \quad .$$

Thus, by setting a to a very large number $J_{rg}(t)|_{inner}$ can analyse cracks under plane strain (but not plane stress) conditions.

From Figure 2.1 it is apparent that as $r \rightarrow r_p$, r_s and $A \rightarrow 0$ and, thus, the integrals over r_s and A vanish. By combining equations (2.26) and (2.27) it is observed that as $r \rightarrow r_p$, the expression for $J_{rg}(t)$ reduces to equation (2.7) because it was assumed that the fracture-process region is contained mainly by essentially flat boundaries in the r-θ plane. Also, from equations (2.26) and (2.27) it is observed that

$$\underset{r \rightarrow r_p}{Lt} J_{rg}(t)|_{inner} \rightarrow \int_{r_p} (W \cos\psi - T_{n_i} \frac{\partial u_i}{\partial r}) \, dr \, ,$$

$$= J|_{\substack{crack \\ tip}} \, , \qquad (2.30)$$

where Rice's integral J is not path independent in axisymmetric problems and has meaning only as the energy flux into the crack tip. Since $J_{rg}(t)$ is path independent, one may write for any r ;

$$J_{rg}(t)|_{inner} = J|_{\substack{crack \\ tip}} \, . \qquad (2.31)$$

2.8 Relation with Dynamic Stress Intensity Factor

In usual elastodynamic crack analyses the effects of body forces are neglected in addition to the disregard

of inelastic strains so that equation (2.29) may be reduced then to

$$J_{rg}(t)\Big|_{\substack{\text{inner}\\\text{outer}}} = \pm\int_{\Gamma}\left((W - \sigma_{rr}\frac{\partial u_r}{\partial r} - \sigma_{rz}\frac{\partial u_z}{\partial r})\cos\psi - (\sigma_{rz}\frac{\partial u_r}{\partial r} + \sigma_{zz}\frac{\partial u_z}{\partial r})\sin\psi\right)\frac{r}{a}\,d\Gamma$$

$$\pm\int_{\Gamma_s} P\frac{\partial u_z}{\partial r}\sin(\psi)\,\frac{r}{a}\,d\Gamma$$

$$\pm\int_{A}\left(\rho(\ddot{u}_r\frac{\partial u_r}{\partial r} + \ddot{u}_z\frac{\partial u_z}{\partial r})\frac{r}{a} + \frac{(\sigma_{\theta\theta}\varepsilon_{\theta\theta} - W)}{a}\right)dA \quad . \qquad (2.32)$$

To obtain a relation between $K_I(t)$ and $J_{rg}(t)$, the axisymmetric field equations describing stresses and displacements near a crack tip, which are written in terms of $K_I(t)$, must be substituted into equation (2.30). This procedure emulates that presented by Rice for planar cases in reference [27]. However, Sih [38]† has shown that a state of plane strain exists at the crack tip. More specifically, from reference [1] one can ascertain that as $R \longrightarrow 0$ these axisymmetric field equations reduce to the same expressions as do their plane strain counterparts. The result of substituting the plane strain field equations into (2.30) is the plane strain relation between K_I and J developed by Rice [27]. Therefore, by means of equations (2.30) and (2.31) one can utilize this plane strain relation for an isotropic material to arrive at

---

† As discussed by Sih in reference [1].

$$K_I(t) = \left(\frac{J_{rg}(t) E}{(1-\nu)^2} \right)^{1/2} . \qquad (2.33)$$

In equation (2.33) E is Young's modulus and ν is Poisson's ratio. The relation between $K_I(t)$ and $J_{rg}(t)$ illustrates the equivalence of using a critical $K_I(t)$ or a critical $J_{rg}(t)$ as a material-property fracture criterion because both parameters are a measure of the energy flux to the crack tip.

2.9 Conclusions

A general path-independent integral describing the energy flux to the crack tip can be formulated for stationary cracks under axisymmetric mode I conditions following the concepts developed for planar cases. This $J_{rg}(t)$-integral can be applied to anisotropic materials and will include the effects of dynamic loads, body forces, thermal strains and plastic strains. Applications are limited to those cases involving a homogeneous material inside the contours for which infinitesimal strain theory is valid. The $J_{rg}(t)$-integral is related to the mode I dynamic stress intensity factor in elastodynamic crack problems.

CHAPTER THREE
FINITE ELEMENT ANALYSIS OF WAVE PROPAGATION IN LINEAR ELASTIC SOLIDS

3.1 Introduction

An elastodynamic finite element computer program based on isotropic material behaviour, TEPSAD, was developed by extending the TEPSA static code [40] to include the influence of material inertia for both axisymmetric and plane strain conditions. Constant-strain elements were employed and the effects of damping were neglected. The essence of the analysis was to treat the dynamic problem as an equivalent static problem at a series of points in time. A set of discretized differential equations of motion were developed by utilizing Hamilton's variational principle, from which resulted the consistent-mass matrix. However, some researchers have found that the lumped-mass matrix must be employed in modelling wave propagation [18,41]. The more economical lumped-mass matrix was applied in this analysis.

The two approaches to solving the equations of motion numerically are the normal mode and the direct time-integration techniques. Descriptions of both methods may be found in references [41-45]. Due to the usual presence of high frequencies in wave propagation, the direct time-integration schemes appear to be more efficient for this

class of problem [41] and, hence this method was adopted. The most popular time-integration techniques are the Newmark β generalized-acceleration method [46] and the Wilson θ linear-acceleration technique [45] which are both unconditionally stable. The Newmark β method has been applied successfully to wave propagation problems by many investigators [17-21,23,24,47,48] and was chosen in this study due to its greater versatility [49].

As a result of the numerical time-integration, the simultaneous differential equations of motion are converted to a set of linear algebraic equations. The system properties are assumed to remain constant and, thus, these linear equations may be solved by an efficient Gaussian elimination matrix-decomposition procedure implemented into the code.

The finite element method is well documented [43,45,50], and the formulations will be presented only briefly here.

3.2 Discretized Equations of Motion

Consider the finite element of surface area, S^e, and volume, V^e, as illustrated in Figure 3.1. By considering only a conservative system in a conservative force field one may formulate the equations of motion by using

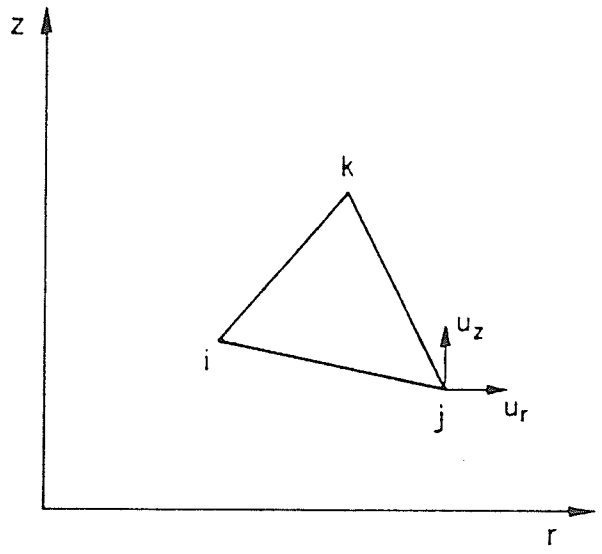

Figure 3.1 - A typical triangular finite element.

Hamilton's variational principle [51]. This principle states that the system's motion is such that the time average of the difference between the kinetic energy, T, and the potential energy, U, will be minimized between any times t_1 and t_2 providing kinetic constraints are satisfied. This time average is written as a functional, Φ, which is made stationary by setting its first variation to zero. Therefore,

$$\delta\Phi = \delta\int_{t_1}^{t_2} (T - U)\, dt = \int_{t_1}^{t_2} (\delta T - \delta U)\, dt = 0 \quad . \tag{3.1}$$

From reference [52],

$$T = \frac{1}{2}\int_{V^e} \rho\dot{\mathbf{u}} \cdot \dot{\mathbf{u}}\, dV \quad , \tag{3.2}$$

and

$$U = \int_{V^e} W\, dV - \int_{S^e} \mathbf{u} \cdot \mathbf{g}\, dS \quad , \tag{3.3}$$

where W is the elastic strain energy density function and $\mathbf{g}$ is a vector of external surface tractions.

The unknowns in equations (3.2) and (3.3) may be discretized in space by expressing them in terms of the values $\{u\}$ and $\{\dot{u}\}$ at the nodes. The displacements are assumed to vary linearly between the nodes,

$$\mathbf{u} = [N]\{u\} \quad , \tag{3.4}$$

where $[N]$ contains the linear interpolation functions. As well, the elastic strain energy density function may be

expressed by

$$W = \frac{1}{2}\{\varepsilon\}^T\{\sigma\} \quad , \tag{3.5}$$

where

$$\{\varepsilon\} = [B]\{u\} \tag{3.6}$$

and

$$\{\sigma\} = [C]\{\varepsilon\} \quad . \tag{3.7}$$

In the above equations $[B]$ is obtained by applying the infinitesimal strain-displacement relations to $[N]$ whilst $[C]$ relates $\{\sigma\}$ and $\{\varepsilon\}$ through Hooke's law.

Equations (3.4) to (3.7) may be substituted into (3.2) and (3.3), which in turn are substituted into (3.1) with the result that

$$\delta\Phi = \int_{t_1}^{t_2} \Bigg(\int_{V^e} \left(\rho\{\delta\dot{u}\}^T[N]^T[N]\{\dot{u}\} - \{\delta u\}^T[B]^T[C][B]\{u\}\right) dV + \int_{S^e} \{\delta u\}^T[N]^T\{g\}\, dS \Bigg) dt = 0 \quad . \tag{3.8}$$

The variations $\{\delta u\}$ are zero at times t_1 and t_2 [51] and $\{\delta\dot{u}\}$ may be eliminated by integrating the first term of equation (3.8) by parts to yield

$$\delta\Phi = \int_{t_1}^{t_2} \{\delta u\}^T \Bigg(- \int_{V^e} \rho[N]^T[N]\, dV\, \{\ddot{u}\} - \int_{V^e} [B]^T[C][B]\, dV\, \{u\} + \int_{S^e} [N]^T\{g\}\, dS \Bigg) dt = 0 \quad .$$

Since the variations are arbitrary [51],

$$\int_{V^e} \rho[N]^T[N]\, dV\, \{\ddot{u}\} + \int_{V^e} [B]^T[C][B]\, dV\, \{u\} = \int_{S^e} [N]^T\{g\}\, dS \quad . \tag{3.9}$$

The element consistent-mass matrix is

$$[M^e] = \int_{V^e} \rho[N]^T[N]\, dV \quad ,$$

the element stiffness matrix is

$$[K^e] = \int_{V^e} [B]^T[C][B]\, dV \quad ,$$

and the element nodal-force vector is given by

$$\{F^e\} = \int_{S^e} [N]^T\{g\}\, dS \quad .$$

From these definitions one may write equations (3.9) as

$$[M^e]\{\ddot{u}\} + [K^e]\{u\} = \{F^e\} \quad .$$

Although $[M^e]$ has been formulated in terms of the continuous element shape functions, the element's mass will be more simply lumped at the nodes instead by using the

technique described in reference [40] for a thermal analysis. This procedure is presented in Appendix V.

The element matrices are assembled according to the direct-stiffness method [50] to form the global system of the equations of motion,

$$[M]\{\ddot{u}\} + [K]\{u\} = \{F\} \ , \tag{3.10}$$

where $[M]$ is a diagonal matrix.

3.3 Direct Time-Integration of the Equations of Motion

The global equations of motion, equations (3.10), may be written in incremental form as

$$[M]\{\Delta\ddot{u}_t\} + [K]\{\Delta u_t\} = \{\Delta F_t\} \ , \tag{3.11}$$

where

$$\Delta u_t = u_{t+\Delta t} - u_t \ , \ . \ . \ . \ \text{etc.}$$

The Newmark β method approximates the displacements and velocities at time $t + \Delta t$ by the recurrence relations [46]

$$\{u_{t+\Delta t}\} = \{u_t\} + \Delta t\{\dot{u}_t\} + \Delta t^2\left(\left(\frac{1}{2} - \beta\right)\{\ddot{u}_t\} + \beta\{\ddot{u}_{t+\Delta t}\}\right) \tag{3.12}$$

and

$$\{\dot{u}_{t+\Delta t}\} = \{\dot{u}_t\} + \Delta t\left((1 - \gamma)\{\ddot{u}_t\} + \gamma\{\ddot{u}_{t+\Delta t}\}\right) \ , \tag{3.13}$$

where β and γ dictate the assumed variation of accelerations (constant, linear, etc.) during the time-step Δt. One may write equation (3.12) in incremental form as

$$\{\Delta u_t\} = \Delta t\{\dot{u}_t\} + \frac{\Delta t^2}{2}\{\ddot{u}_t\} + \Delta t^2 \beta\{\Delta \ddot{u}_t\} \quad . \tag{3.14}$$

Equation (3.14) can be rearranged to give

$$\{\Delta \ddot{u}_t\} = \frac{1}{\beta}\left(\frac{1}{\Delta t^2}\{\Delta u_t\} - \frac{1}{\Delta t}\{\dot{u}_t\} - \frac{1}{2}\{\ddot{u}_t\}\right) \quad . \tag{3.15}$$

By substituting equations (3.14) and (3.15) into (3.11) and rearranging, one has

$$\left([K] + \frac{1}{\beta \Delta t^2}[M]\right)\{\Delta u_t\} = \{\Delta F_t\} + [M]\left(\frac{1}{\beta \Delta t}\{\dot{u}_t\} + \frac{1}{2\beta}\{\ddot{u}_t\}\right) \quad , \tag{3.16}$$

or,

$$[\tilde{K}]\{\Delta u_t\} = \{\Delta \tilde{F}_t\} \quad .$$

The $[\tilde{K}]$ is the effective global stiffness matrix and $\{\Delta \tilde{F}_t\}$ is the effective global nodal-force-increment vector. Thus, the task of solving a set of simultaneous second-order differential equations has been reduced to that of solving a system of simultaneous linear algebraic equations. Once $\{\Delta u_t\}$ has been computed, other quantities can be determined from the recurrence relations and the whole procedure can be repeated at the next instant.

3.4 Initial Conditions and Applied Loads

As with the solution of any second-order differential equation, two initial conditions are required to start the time-integration algorithm. The two conditions chosen are $\{\dot{u}_{t=0}\}$ and $\{u_{t=0}\}$ which, when substituted into equation (3.10), may be used to solve for $\{\ddot{u}_{t=0}\}$ by using

$$\{\ddot{u}_{t=0}\} = [M]^{-1}(\{F_{t=0}\} - [K]\{u_{t=0}\}) \quad .$$

The computational economy of using a lumped-mass matrix is clearly apparent from this last relationship.

The components of $\{g\}$ accommodate only normal surface tractions and are separated in time and space.

3.5 Matrix-Decomposition Equation Solver

By fixing the structural properties and time-step size throughout an analysis, the effective stiffness matrix remains constant. Thus, Gaussian elimination need be performed on this matrix only at the first time-step. Since $[\tilde{K}]$ is symmetric, the matrix is decomposed as

$$[\tilde{K}] = [L][D][L]^T \quad ,$$

where $[L]$ is a lower triangular matrix and $[D]$ is a diagonal matrix. This particular decomposition technique was chosen over the closely related Cholesky method to realize a small

saving in numerical operations [53]. On the first and all subsequent time-steps, an intermediate vector $\{Y\}$ is determined by using forward substitution, or

$$[L][D]\{Y\} = \{\Delta\tilde{F}_t\} \quad .$$

Once $\{Y\}$ has been found the displacement increments are determined by back substitution from

$$[L]^T\{\Delta u_t\} = \{Y\} \quad .$$

CHAPTER FOUR

EXAMPLE PROBLEMS

4.1 Wave Propagation in Smooth Solids

Prior to performing axisymmetric crack analyses, the finite element computer code TEPSAD was tested on problems involving wave propagation in linear elastic solids[†] containing no cracks. Results were compared with those from other solutions. In addition to modelling axisymmetric problems, a case under plane strain conditions was also investigated to further test general program functions and to demonstrate more completely the capabilities of the code.

In all cases the Newmark numerical time integration parameters were $\beta = 0.25$ and $\gamma = 0.50$ for which no damping is inherent in the numerical time-integration [46]. To minimize the error in the time-integration, the time-step size was chosen such that the dilatational wave would travel across the smallest element in the mesh during one time increment [18].

4.1.1 Case 1: A Long Thick-Walled Cylinder Subjected to a Sudden Internal Pressure

A thick-walled cylinder with an assumed infinite length, such that plane strain conditions prevail along

---

[†] A comprehensive introduction to stress wave propagation in solids is presented in reference [54].

its principal axis, is depicted by its cross section in Figure 4.1. The wall thickness is given by $r_2/r_1 = 2.0$, and Poisson's ratio is 0.3 . The cylinder was subjected to a spatially uniform internal pressure given by

$$P(t) = P_o H(t) \quad ,$$

where P_o is the applied pressure[†] and $H(t)$ is the unit Heaviside step function. The finite element model consists of 32 equal-sized square elements along the radial direction which produces 66 nodes.

The normalized hoop stress, $\sigma_{\theta\theta}/P_o$, is presented as a function of non-dimensionalized time in Figure 4.2. The result from TEPSAD at $r = 1.031r_1$[††] is compared with an approximate analytical solution presented in reference [48] at $r=r_1$.

The TEPSAD result exhibited very small oscillations through which the dashed curve was faired. The code displayed good accuracy in modelling the reinforcement of the stress wave reflected from the outside wall at c_1t/r_1 equal to 2.0 and 4.0 . The curves follow a downward trend for $c_1t/r_1 > 5$, when the cylinder tended to static equilibrum.

[†] In all case studies the numerical value of a compressive pressure shall possess a positive sign.

[††] The constant-strain elements in the TEPSAD code limit the code to computing stresses at the centroids of the elements. Thus, stresses at exact boundaries cannot be determined.

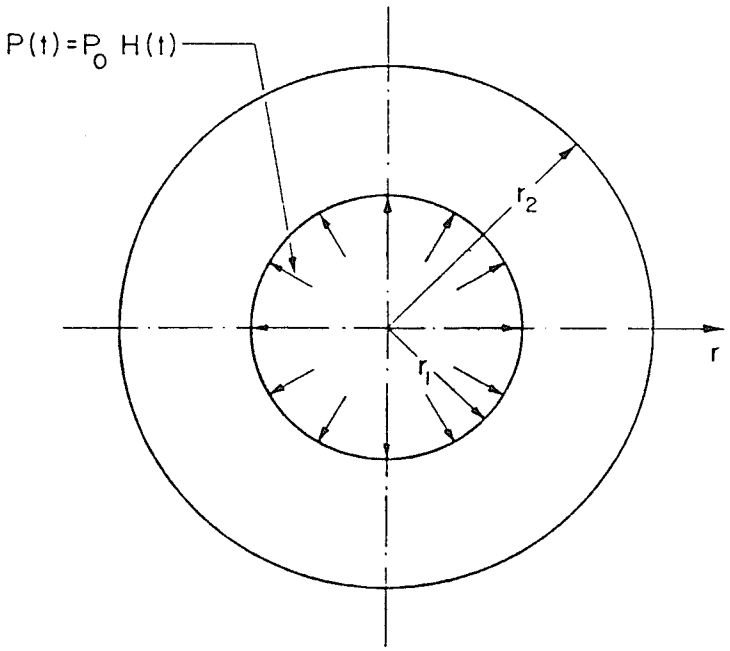

Figure 4.1 - An internally pressurized thick-walled circular cylinder.

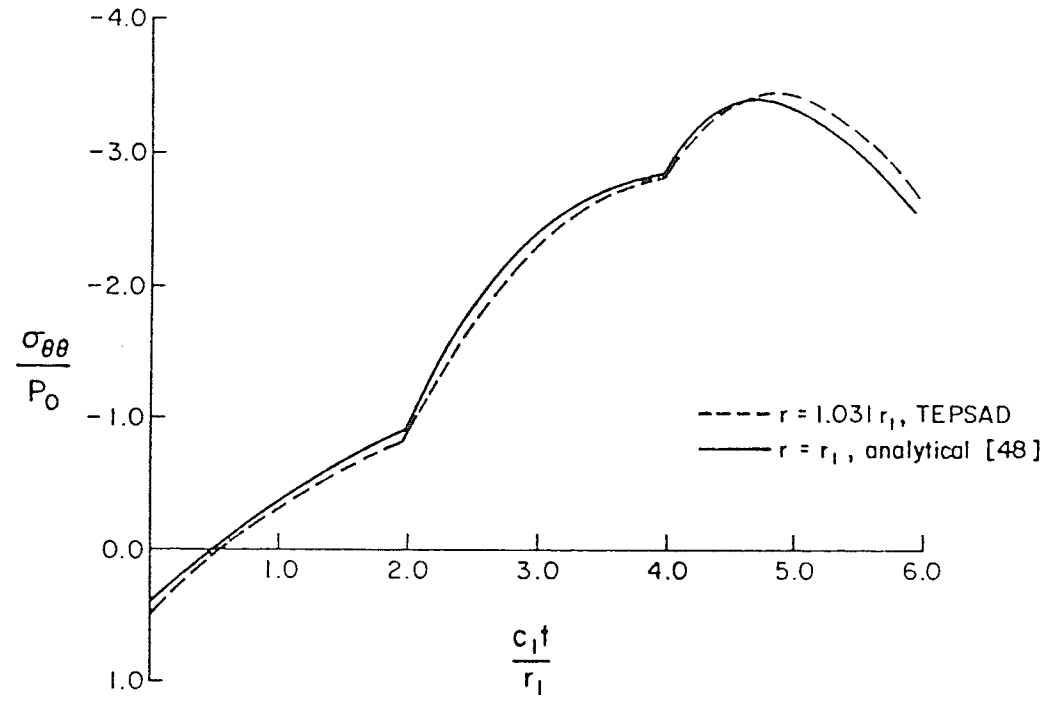

Figure 4.2 - Variation of the normalized hoop stress, $\sigma_{\theta\theta}/P_o$, with non-dimensionalized time at the nominal radius $r = r_1$ in the internally pressurized thick-walled cylinder.

4.1.2 Case 2: A Solid Cylinder Subjected to a Sudden End Loading

This case tested the performance of the code in modelling two-dimensional axisymmetric problems. A solid circular cylinder of finite length is illustrated in Figure 4.3, where $r_2/L = 0.25$ and Poisson's ratio is 0.3 . One end of the cylinder was subjected to a uniform pressure following a ramp function having the non-dimensionalized time dependence given in Figure 4.4. The cylinder was discretized using a uniform grid with 5 square elements in the r-direction and 20 square elements in the z-direction which makes a total of 126 nodes.

Results are compared in Figures 4.5 to 4.9 to those produced by Biffle [48], where the same mesh was employed, but the problem was solved by linearly interpolating stresses rather than displacements between element nodes. As well, a consistent-mass matrix was used in [48]. As in [48], the magnitudes of the shear stress σ_{rz} were quite small, and are not presented.

In Figures 4.5 and 4.6 are presented the normalized axial stress, σ_{zz}/P_o , as a function of non-dimensionalized time at the axial locations $z = 0.25L$, $z = 0.75L$ at the nominal radii† $r = 0$ and $r = r_2$, respectively. The early arrival time of the dilatational

† The TEPSAD code computed stresses at the centroids of elements adjacent to the axis of symmetry at $r = 0$ and at the surface at $r = r_2$.

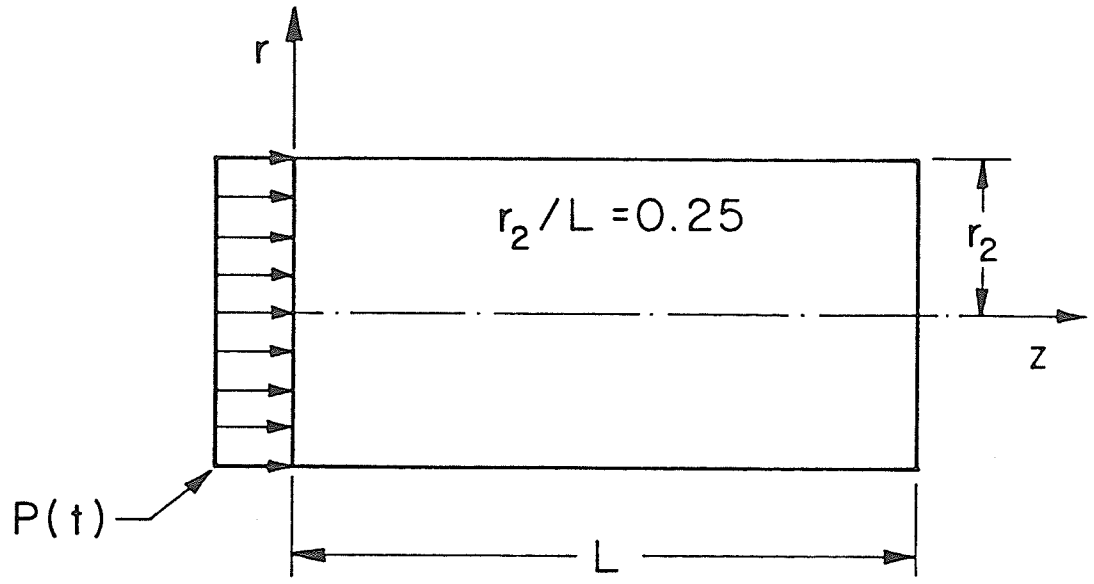

Figure 4.3 - A solid circular cylinder subjected to an end loading.

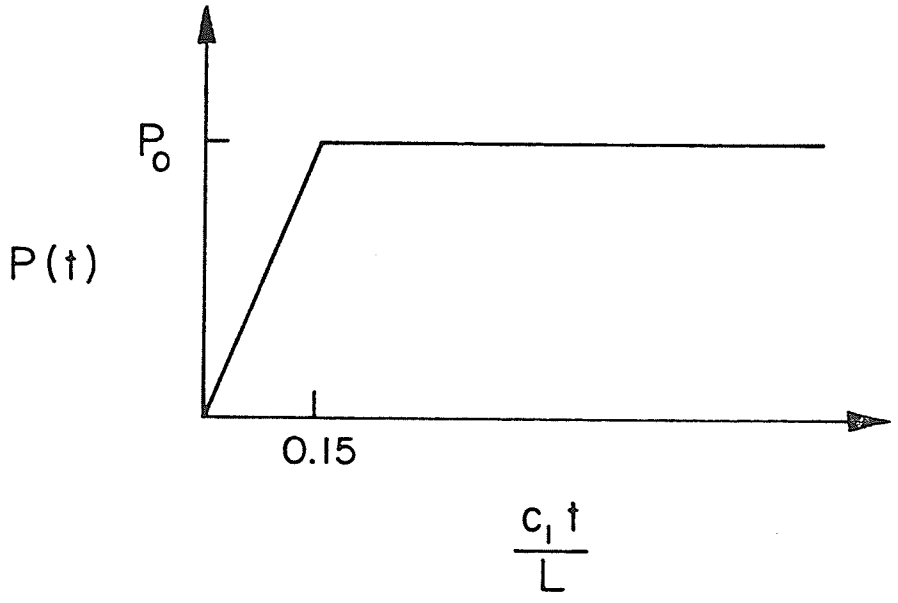

Figure 4.4 - Dependence of end loading on the solid cylinder on non-dimensionalized time.

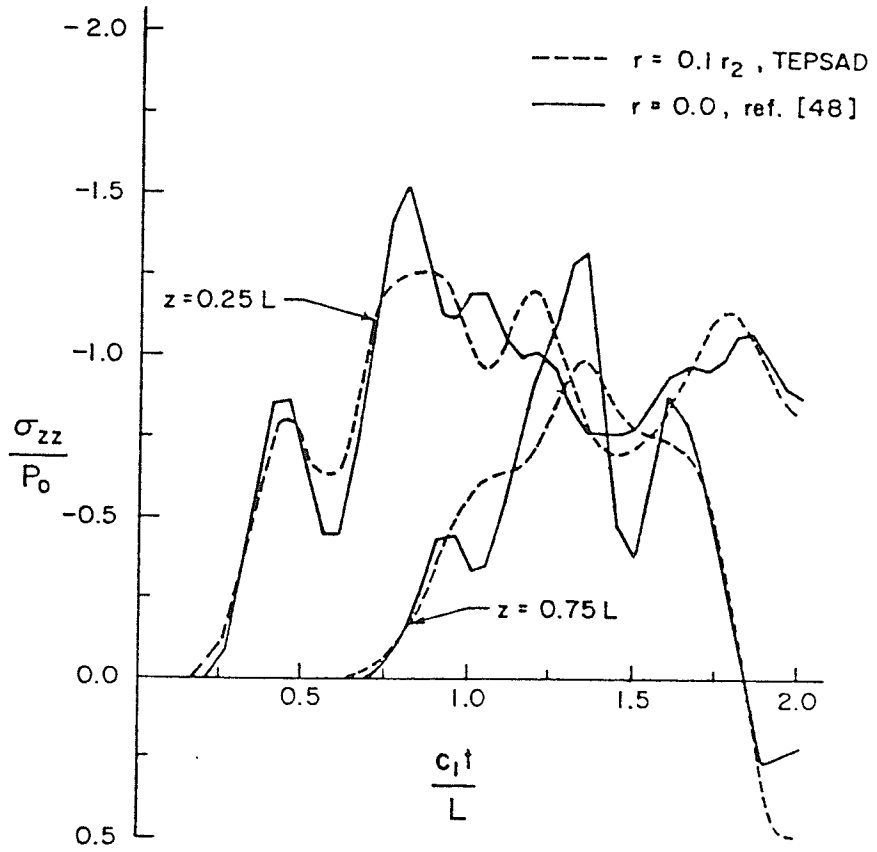

Figure 4.5 - Variation of the normalized axial stress, σ_{zz}/P_o, with non-dimensionalized time at the nominal radius $r = 0$ in the solid cylinder.

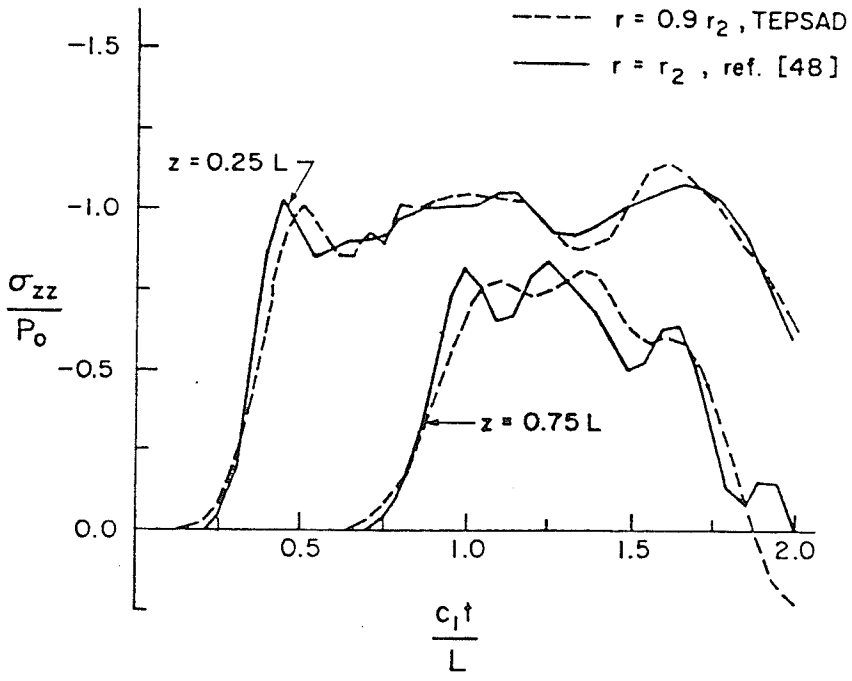

Figure 4.6 - Variation of the normalized axial stress, σ_{zz}/P_o, with non-dimensionalized time at the nominal radius $r = r_2$ in the solid cylinder.

wave in the TEPSAD solution is attributed to the presence of artificial farfield-coupling and discretization dispersion of nodal displacements [55] which is inherent in the constant-strain, lumped-mass finite element method. One effect of these two related mechanisms is the propagation of the stress waves at speeds greater than the theoretical continuum wave speeds, c_1 and c_2. This effect becomes greater at higher frequencies as seen in this case.

In Figure 4.5 the decrease in the initial rise of σ_{zz}/P_o at $z = 0.25L$ indicates the arrival of a tensile wave formed from a surface reflection. Both solutions display the focusing of stress waves converging on the cylinder's centreline with the TEPSAD results peaking at lower stress levels. These discrepancies in the two solutions can be partially attributed to the non-zero radial position for the TEPSAD results as well as the lesser ability of the lower-order TEPSAD elements to model the high stress gradients near the cylinder's centreline. In the region adjacent to the outer surface of the cylinder, the stress waves travelling in the radial direction are defocused such that their influence is small compared to the waves travelling directly in the z-direction. Thus, Figure 4.6

illustrates a closer match between the two solutions.

Plotted in Figure 4.7 are the non-dimensionalized time histories of σ_{rr}/P_o and $\sigma_{\theta\theta}/P_o$, where $\sigma_{rr}/P_o = \sigma_{\theta\theta}/P_o$, at the locations $z = 0$ (nominally) and $z = 0.5L$, at the nominal radius $r = 0$. In Figure 4.8 is presented $\sigma_{\theta\theta}/P_o$ as a function of non-dimensionalized time at the locations $z = 0$ (nominally) and $z = 0.5L$, at the nominal radius $r = r_2$. Reasonable agreement between the two solution techniques is observed in both figures. Stress oscillations about zero illustrate the radial movement of the stress waves reflecting back and forth between $r = 0$ and $r = r_2$. A comparison of Figures 4.7 and 4.8 again show the focusing of the stress waves near $r = 0$. A characteristic, common to Figures 4.5 to 4.7, is the expected result of the solutions from reference [48] and TEPSAD drifting apart with increasing non-dimensionalized time.

In Figure 4.9 is shown the variation of σ_{zz}/P_o with non-dimensionalized distance along the nominal radius $r = r_2$. The plot is at the non-dimensionalized time when the dilatational wavefront has just reached the far end of the cylinder ($c_1 t/L = 1.0$). This wave profile illustrates that the stress wave has become dispersed due to numerical error and the presence of the finite outer boundary of the cylinder.

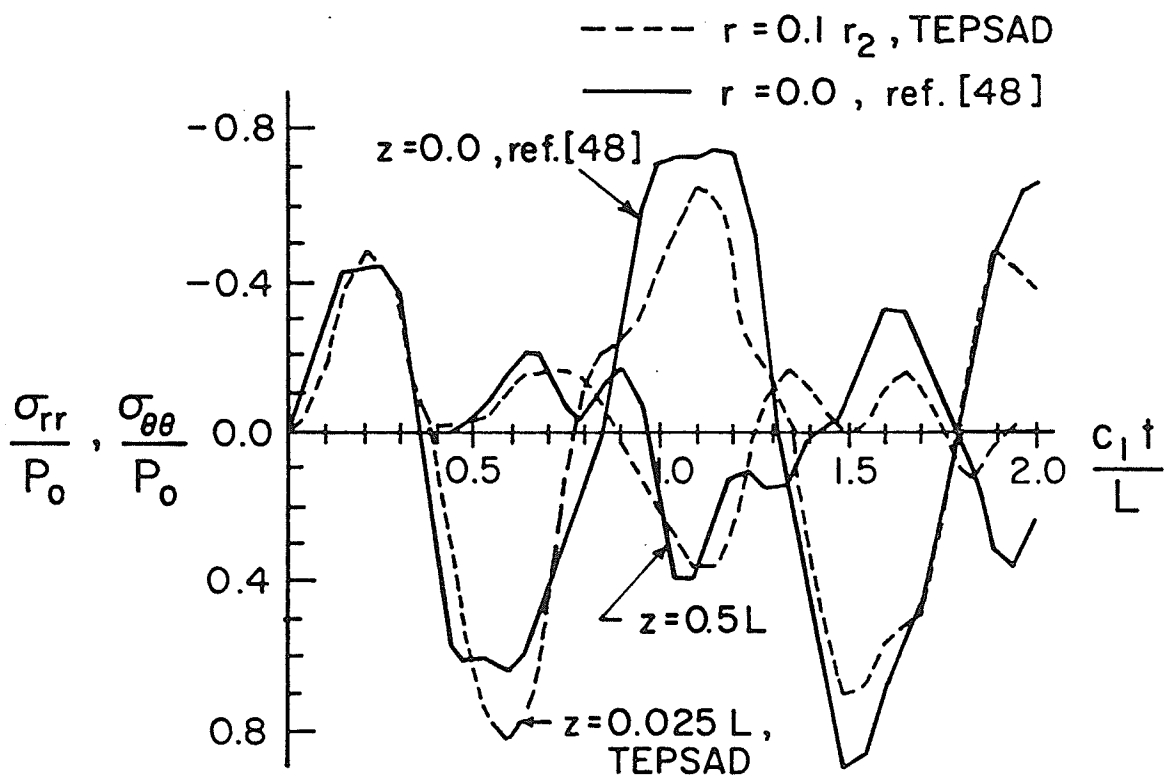

Figure 4.7 - Variations of the normalized radial stress, σ_{rr}/P_o , and the normalized hoop stress, $\sigma_{\theta\theta}/P_o$, with non-dimensionalized time at the nominal radius $r = 0$ in the solid cylinder.

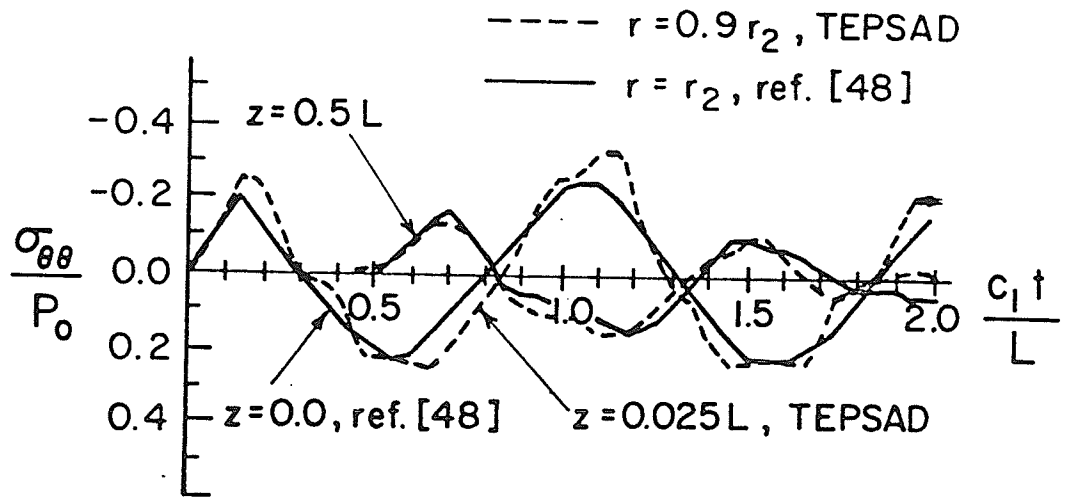

Figure 4.8 - Variation of the normalized hoop stress, $\sigma_{\theta\theta}/P_o$, with non-dimensionalized time at the nominal radius $r = r_2$ in the solid cylinder.

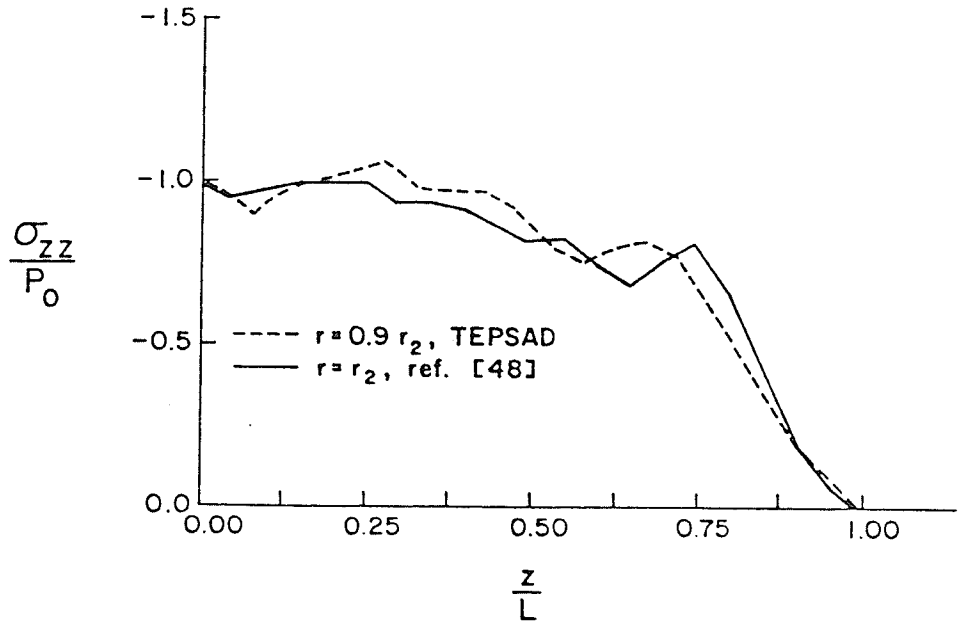

Figure 4.9 - Variation of the normalized axial stress, σ_{zz}/P_o, along the nominal radius $r = r_2$ in the solid cylinder at $c_1 t/L = 1.0$.

By considering the small differences in locations at which stresses were computed in the two solution techniques and the unknown quantity of error in the solution from reference [48], the TEPSAD code appears to produce reasonable results in modelling axisymmetric two-dimensional stress wave propagation.

4.1.3 Case 3: A Semi-Infinite Half-Space Subjected to a Triangular Load

Advantage was taken of one of the few available analytical solutions to a two-dimensional problem to test the TEPSAD code in modelling plane strain structures. The problem is illustrated in Figure 4.10. A distributed triangular load was applied symmetrically between $x = -L$ and $x = +L$ and varied in time according to the ramp function $P(t) = P_o c_1 t/9L$. Poisson's ratio is 1/3 .

Due to symmetry, only one-half of the problem was modelled numerically. The finite element grid is presented in Figure 4.11 and consists of 175 elements and 175 nodes, with zero displacements in the x-direction specified along the boundary $x = 0.0$.

A relatively fine grid was employed in the region near the applied load to accommodate the local high stress gradients. The distributed triangular load was approximated as being constant over a given element. The duration of the

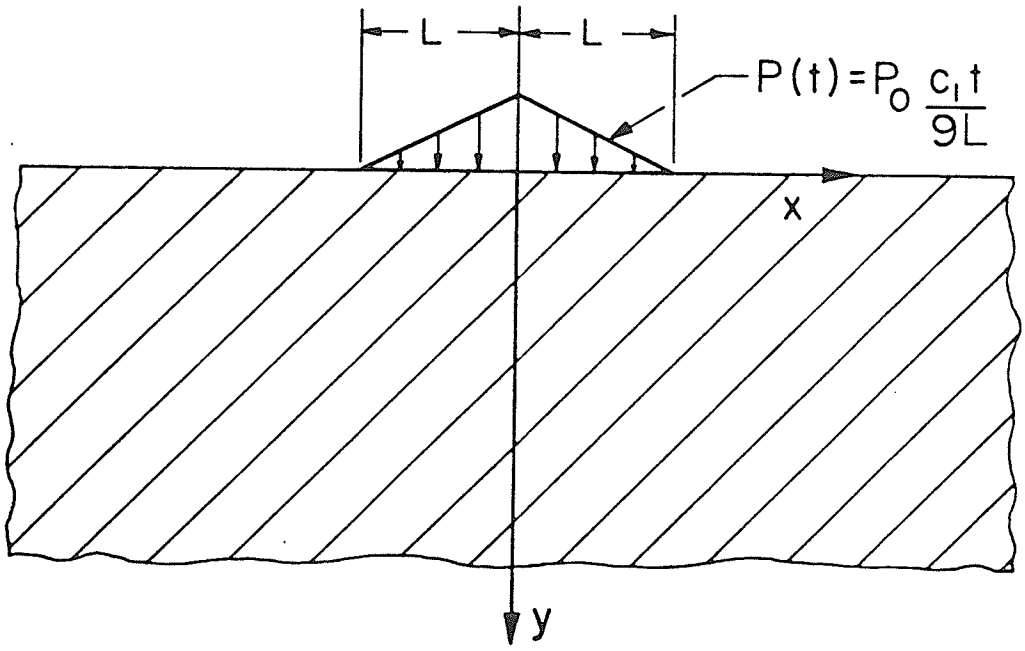

Figure 4.10 - A semi-infinite half-space subjected to a triangular load.

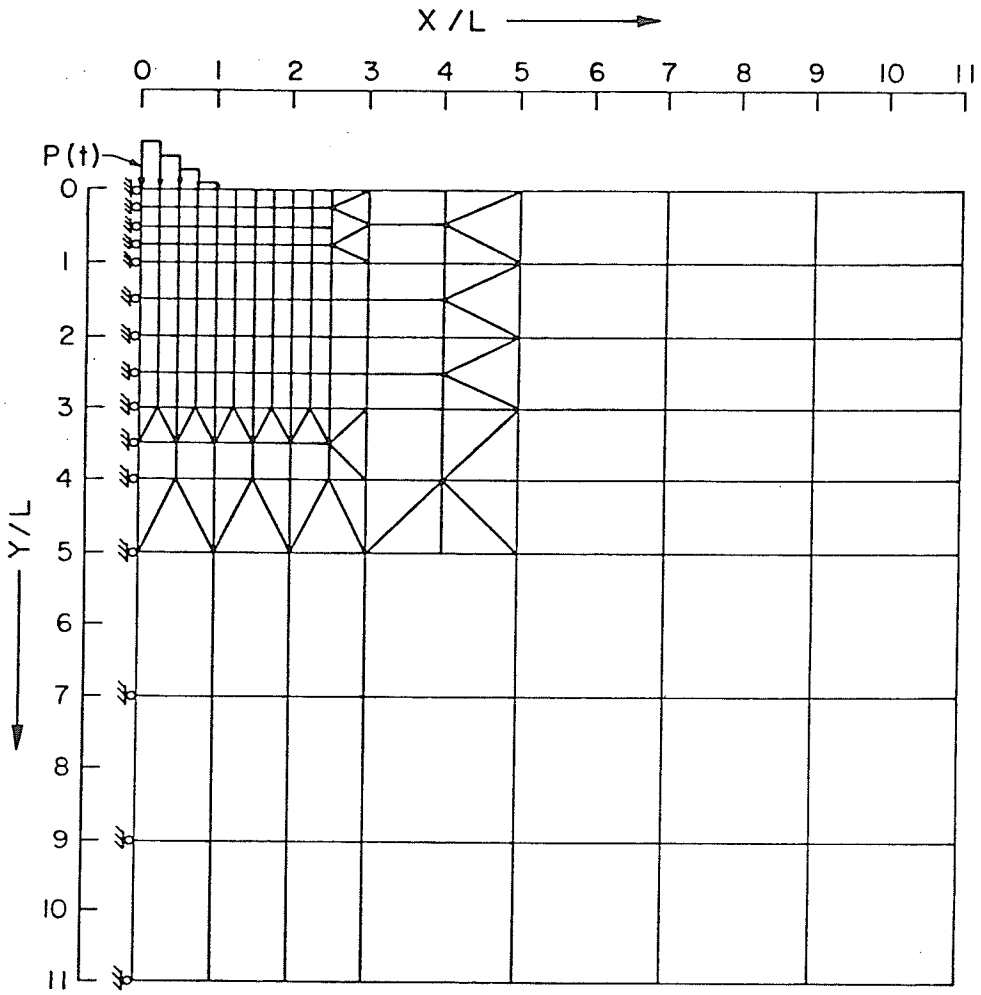

Figure 4.11 - Finite element model of the semi-infinite half-space.

analysis was up to the non-dimensionalized time of $c_1 t/L = 9.0$. At this time the theoretical dilatational wavefront had not yet reached the boundaries $x = 11.0L$ and $y = 11.0L$ which were supposedly at infinity.

Results from the TEPSAD code are shown in Figures 4.12 to 4.14 along with an approximate analytical solution presented by Verner and Becker [47]. In Figure 4.12 are the normalized cartesian stress components, σ_{ij}/P_o , against x/L along $y = 2.0L$ at the non-dimensionalized time $c_1 t/L = 6.0$. As expected, the maximum value of σ_{yy}/P_o occurred directly beneath the peak of the distributed load at $x = 0.0$. The normalized shear stress σ_{xy}/P_o was zero at $x = 0.0$, a consequence of the sliding boundary condition. As well, the slower shear wave given by σ_{xy}/P_o lagged behind the two dilatational waves. The variations of σ_{xx}/P_o , σ_{yy}/P_o and τ_{max}/P_o (where τ_{max} is the maximum shear stress) with non-dimensionalized time are presented in Figure 4.13 at $x = 0.0$, $y = 2.0L$. The early arrival of the TEPSAD computed wavefronts is due to artificial farfield-coupling and discretization dispersion, as mentioned in Case 2. Figure 4.14 presents the non-dimensionalized time histories of the normalized stresses σ_{ij}/P_o at the position $x = 2.0L$, $y = 2.0L$. The ordinate scale in this figure is expanded by a factor of two relative to the previous two figures. The errors in the TEPSAD solution in Figure 4.14 are of the same magnitude as the errors in Figures 4.12 and 4.13.

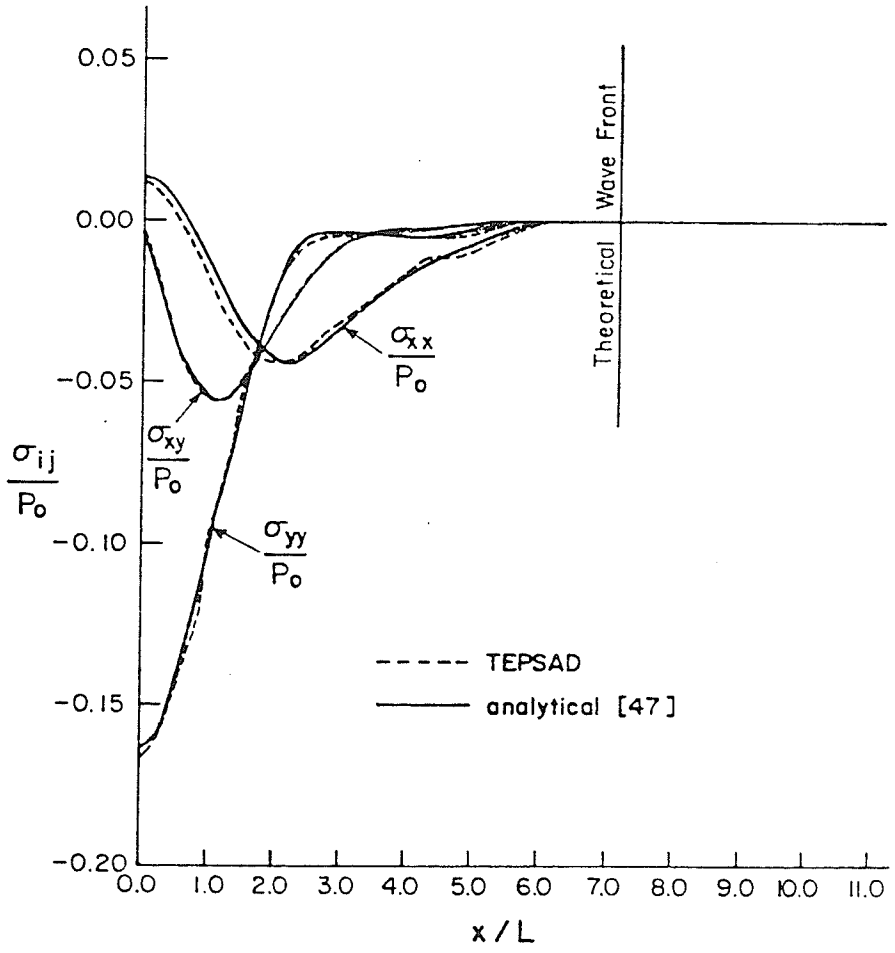

Figure 4.12 - Variations of the normalized cartesian stress components, $\sigma_{ij}/|P_o|$, along $y = 2L$ in the semi-infinite half-space at the non-dimensionalized time $c_1 t/L = 6.0$.

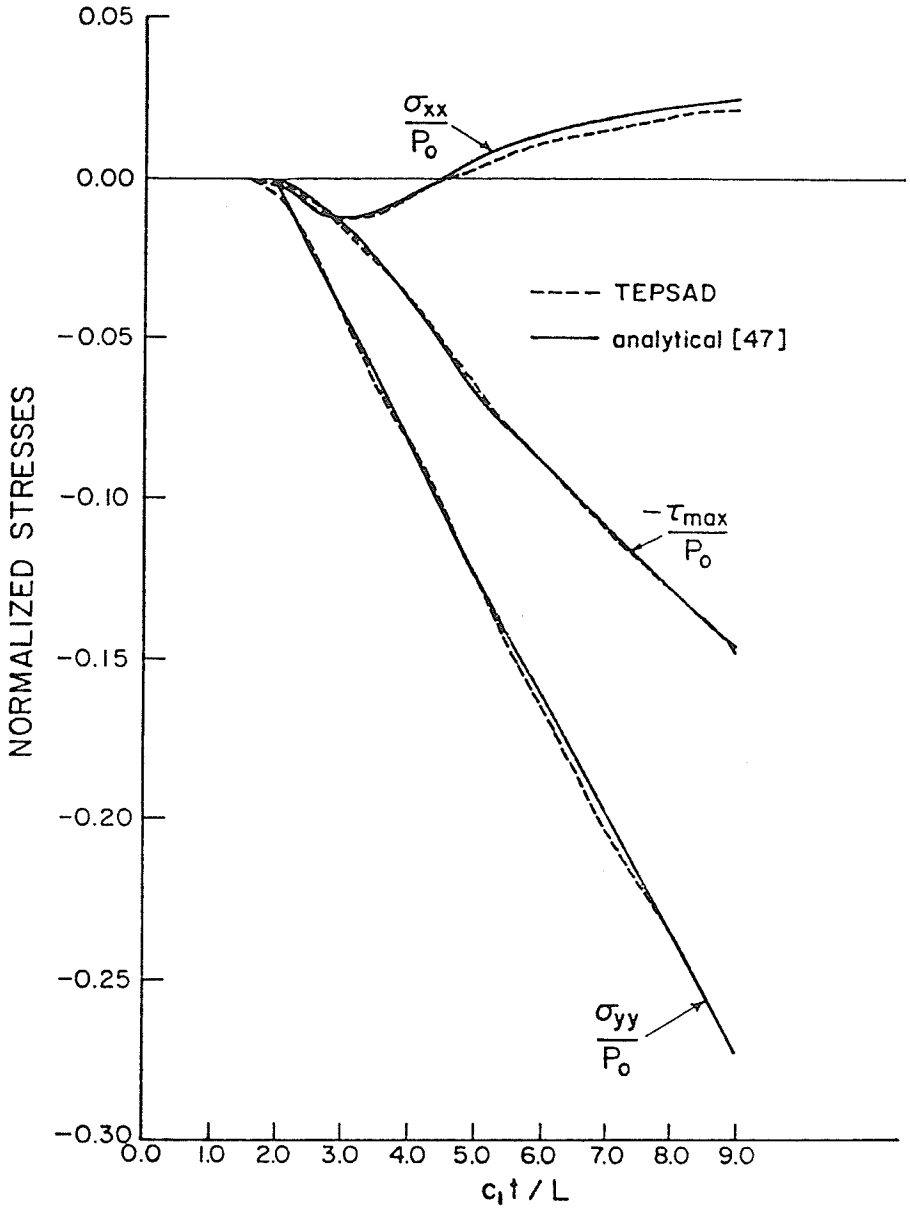

Figure 4.13 - Variations of the normalized stresses $\sigma_{xx}/|P_o|$, $\sigma_{yy}/|P_o|$ and $\tau_{max}/|P_o|$ with non-dimensionalized time at $x = 0$ and $y = 2L$ in the semi-infinite half-space.

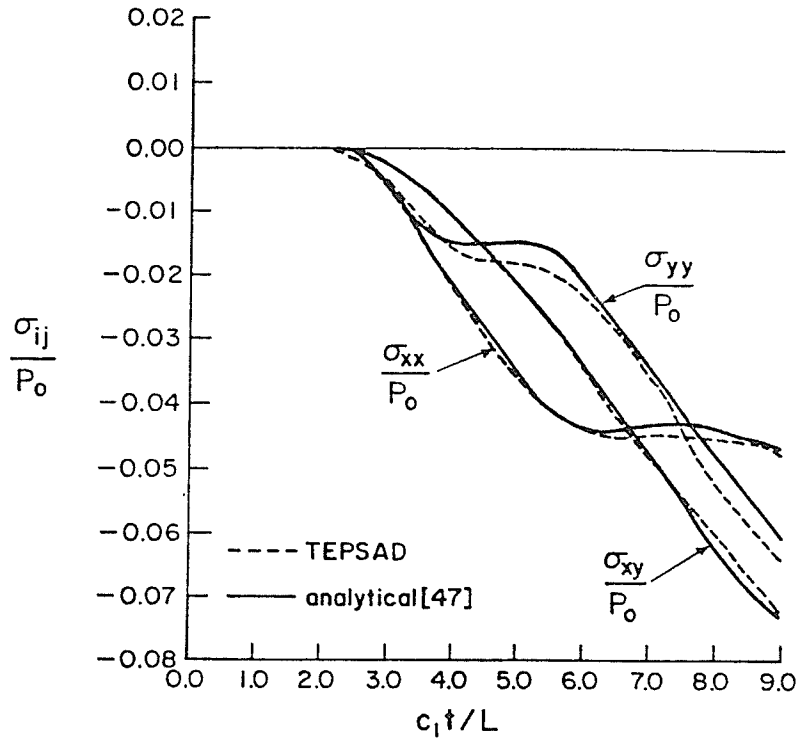

Figure 4.14 - Variations of the normalized cartesian stress components, $\sigma_{ij}/|P_o|$, with non-dimensionalized time at $x = 2L$ and $y = 2L$ in the semi-infinite half-space.

The generally close agreement between the two solutions is attributed to factors not found in Case 2. With the exception of the line of symmetry, $x = 0.0$, the problem is free of reflections from boundaries. As well, stresses in the TEPSAD solution were computed at the exact locations used by the analytical solution. Also, the TEPSAD solution was compared against an approximate analytical solution rather than another numerical solution. It was observed that the TEPSAD solution was in generally closer agreement than the numerical solution of [47] which was produced with the plane strain version of the linear-stress, consistent-mass finite elements [48] mentioned in Case 2.

4.2 Axisymmetric Elastodynamic Crack Problems

Equations (2.32) and (2.33) were implemented into the TEPSAD finite element code. The time history of the dynamic stress intensity factor was determined for linear elastic solid- and thick-walled cylinders containing inner stationary cracks. Results are compared with those from other solution techniques.

The numerical integration of equation (2.32) in the TEPSAD code is based on the summation of finite increments $\Delta\Gamma$ and ΔA, where an increment encompasses one finite element. The integrand is evaluated at the centre of the increment and is assumed to remain constant over the

increment. Spatial derivatives are approximated by finite differences between adjacent nodes. Only rectangular elements are used in the region of integration and r passes through the centroids of these elements. The contour was chosen to be rectangular in shape and was based on the problems being symmetric with respect to the r-θ plane. The Newmark β integration parameters and time-increment criterion were the same as those used in Section 4.1.

4.2.1 Case 4: A Solid Cylinder Containing a Suddenly Pressurized Penny-Shaped Crack

The only elastodynamic axisymmetric crack problem for which a solution was known to the author[†] was used for the first test of the elastodynamic version of the $J_{rg}(t)$-integral (equation (2.32)) and the numerical integration of $J_{rg}(t)$ in the TEPSAD code. A solid circular cylinder of radius r_2 and length $2L$, containing at the centre a penny-shaped crack of tip radius a and zero thickness, is illustrated in Figure 4.15. The geometry is given by $r_2/L = 0.682$ and $a/r_2 = 0.600$ and Poisson's ratio is 0.29. The crack surfaces (at $z = 0^{\pm}$) were subjected to a compressive stress P_o which had a unit Heaviside step-function time dependence.

[†] Reference [1] presents an axisymmetric solution for an infinite medium which is only a special case of the finite cylinder, where $r_2 \rightarrow \infty$.

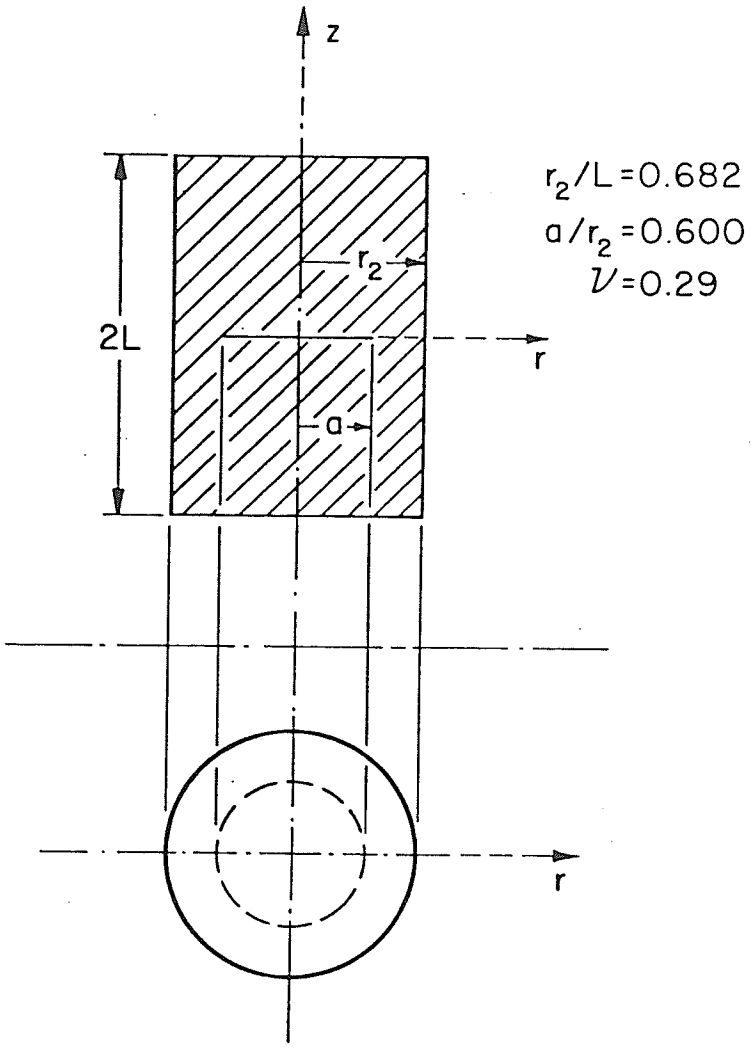

Figure 4.15 - A solid circular cylinder containing a penny-shaped crack.

The problem is symmetric with respect to the crack plane and only the upper-half† of the cylinder was modelled, as illustrated in Figure 4.16. Zero displacements in the z-direction were specified along the ligament ($a \leq r \leq r_2$) at $z = 0$. The finite element model consists of a uniform grid of 330 square elements and 368 nodes. The element size, Δl, is equal to $a/9$. The grid was uniform to minimize the variations in discretization errors for different integration contours. The grid size is very coarse relative to the theoretically high stress gradients near the crack tip, with the ligament consisting of only 6 elements. Thus, the computation of $K_I(t)$ by means of the $J_{rg}(t)$-integral was evaluated under stringent conditions. The coarse grid is due to the limit on the number of degrees of freedom in the TEPSAD code. The $J_{rg}(t)$-integral was computed by using the four different contours illustrated as the dashed lines in Figure 4.16 to test the integral's path independence.

In Figures 4.17a and 4.17b is presented the normalized mode I dynamic stress intensity factor, $\bar{K}_I(t)$, at various non-dimensionalized times, $c_1 t/L$, computed by using the four contours. Normalization was performed by using

---

† The $J_{rg}(t)$-integral subroutines in the TEPSAD code were written only for problems which are symmetric with respect to the plane in which the crack lies. This was to save the required number of degrees of freedom only. Equation (2.32) can be programmed in a similar manner for non-symmetric mode I problems.

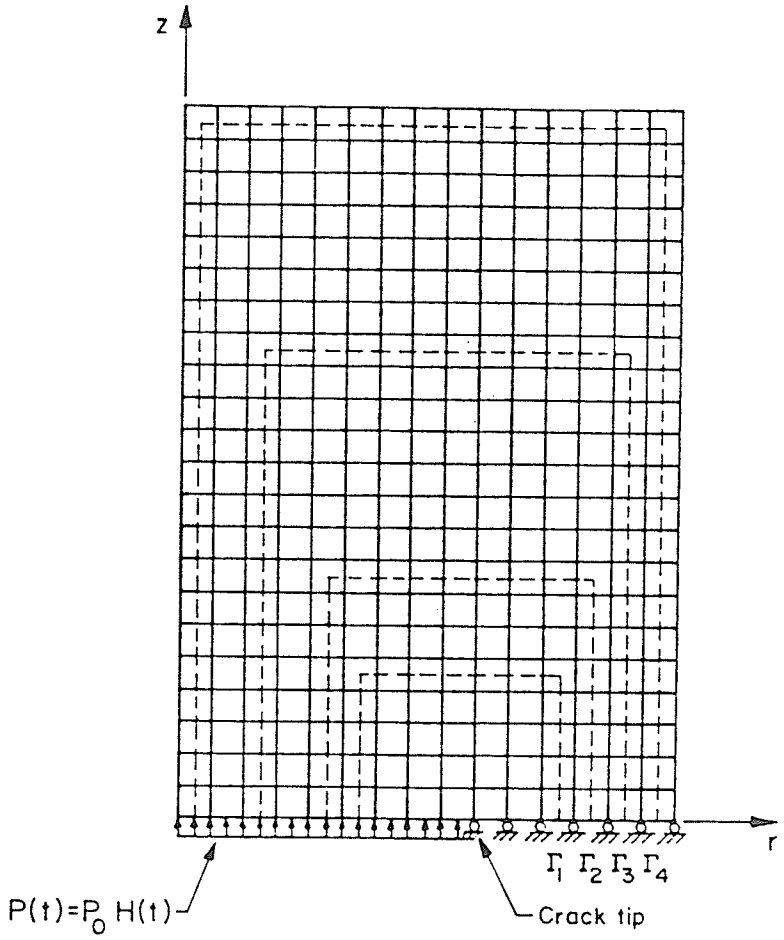

Figure 4.16 - Finite element model of the cracked solid cylinder with the $J_{rg}(t)$-integral contours as illustrated.

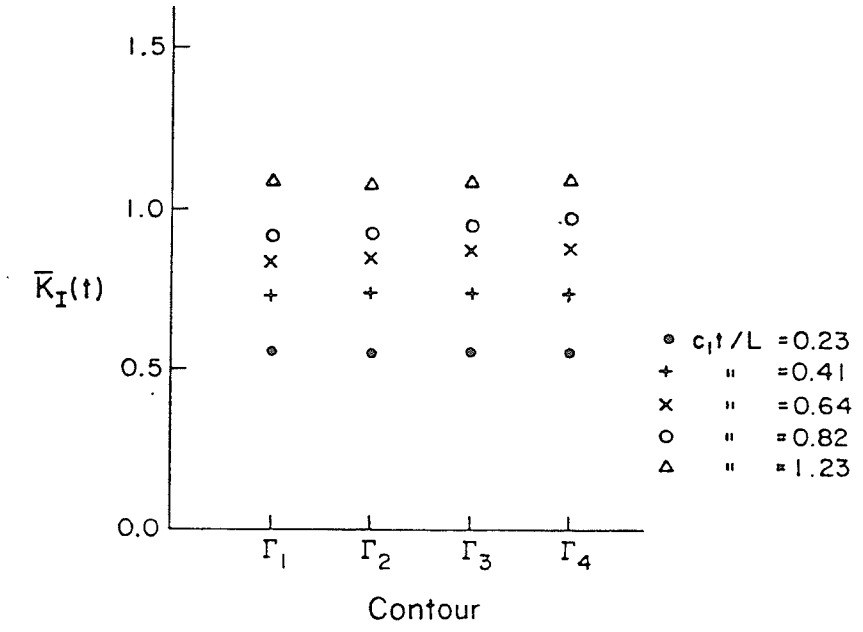

Figure 4.17a

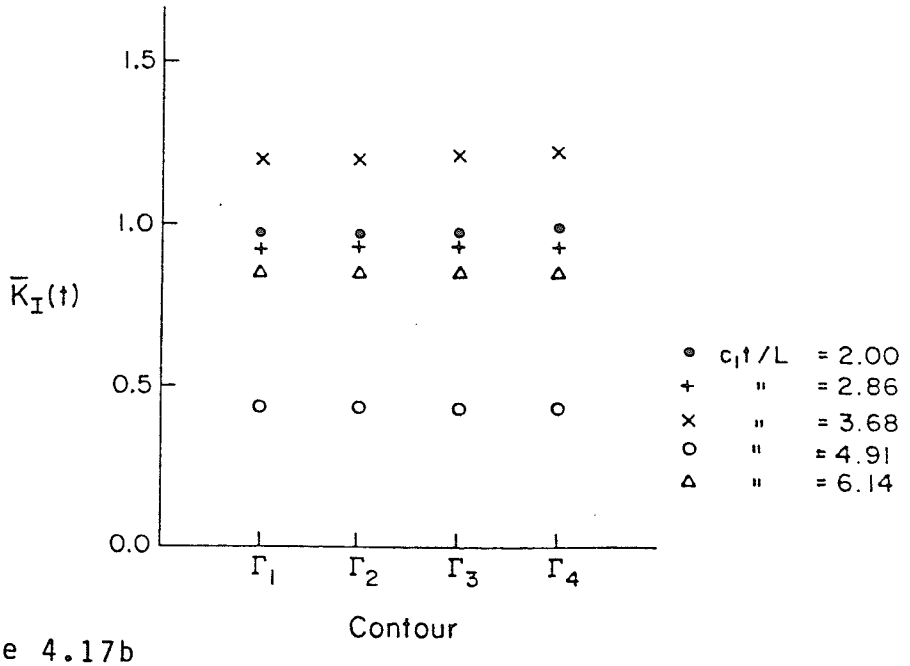

Figure 4.17b

Figures 4.17a - Illustration of the path independence
4.17b of the $J_{rg}(t)$-integral computation of $\bar{K}_I(t)$ for the cracked solid cylinder.

$$\bar{K}_I(t) = \frac{K_I(t)}{K_{I_s}} \quad , \tag{4.1}$$

where K_{I_s} is the static stress intensity factor (arising from the load P_o being applied under static equilibrum). The K_{I_s} is given in reference [13] as $2.25P_o\sqrt{a/\pi}$. Figure 4.17a illustrates the initial rise of $\bar{K}_I(t)$ while Figure 4.17b presents values throughout the remainder of the transient. It is apparent from both figures that the $J_{rg}(t)$-integral is path independent for this case. The largest deviation from path independence occurred at $c_1 t/L = 0.82$, at which $\bar{K}_I(t)$ computed by using Γ_4 is 6.5% of the mean value greater than that computed using Γ_1 . These small differences in $\bar{K}_I(t)$ are attributed to errors inherent in the discretization of both the field solution and the numerical integration of $J_{rg}(t)$.

In Figure 4.18 is presented the non-dimensionalized time history of $\bar{K}_I(t)$ computed by using the contour Γ_2 . Due to the path independence, plots from using the remaining contours were omitted. Also shown in Figure 4.18 is an analytical solution for a cylinder of infinite length presented by Chen [13]. The analytical solution is valid up to the theoretical time the stress wave reflected from the free end reached the crack tip, at $c_1 t/L = 2.00$. The maximum value of the initial rise of $\bar{K}_I(t)$ (which occurred

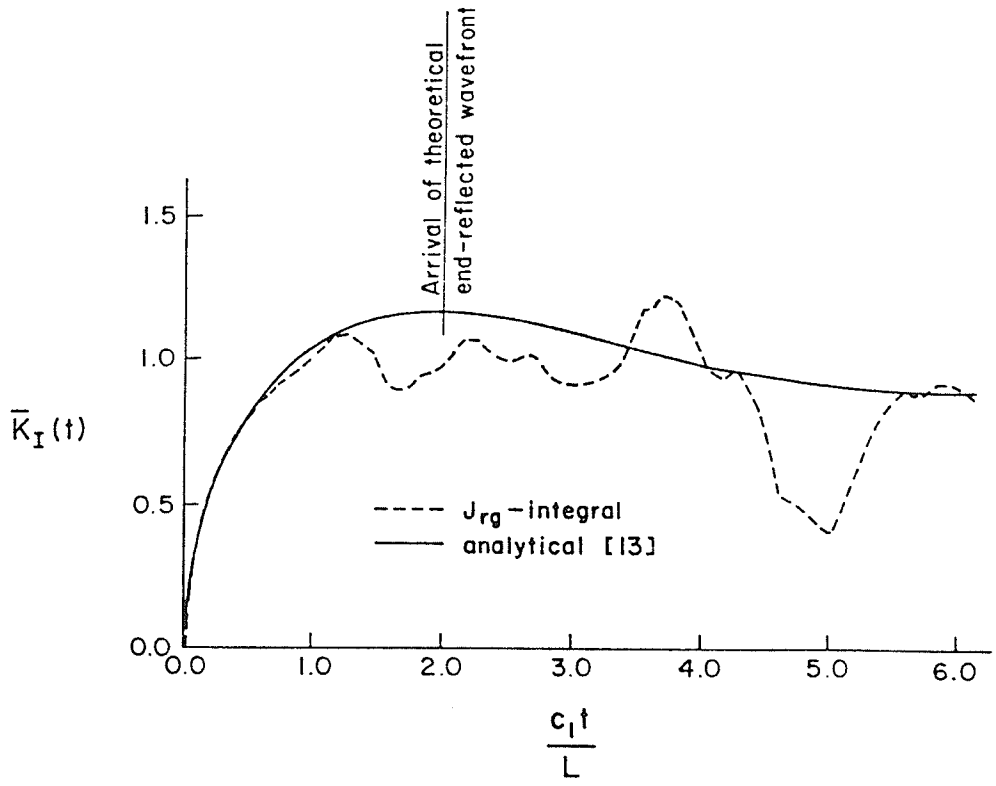

Figure 4.18 - Variation of $\bar{K}_I(t)$ with non-dimensionalized time for the cracked solid cylinder.

during $c_1 t/L < 2.00$) in the numerical solution is lower than that from the analytical solution and occurred at an earlier time. This behaviour is attributed to the finite element solution for the problem. It was found that the major contribution to computing $\bar{K}_I(t)$ was from the integral along the crack-surface contour, Γ_s, which is the second term in equation (2.32). This integral is a function of the crack profile in the r-z plane. By modelling the cylinder using coarse elements based on linear displacement functions, the region near the crack tip, including the crack profile, was unduly constrained against movement. Such constraint resulted in the numerical model being stiffer than the analytical model. Thus, the numerically computed displacements along the crack profile were smaller and oscillated at a higher dominant frequency.

The effect of the finite length of the cylinder is seen in the large oscillations in $\bar{K}_I(t)$ in the numerical solution. The peak value of 1.21 for $\bar{K}_I(t)$ occurred at $c_1 t/L = 3.72$, which corresponded to the arrival time (based on the TEPSAD-generated wave speed being slightly higher than c_1) of the initial compressive wavefront after two reflections from the free end. The returning wave was tensile and, thus, caused the peak in $\bar{K}_I(t)$.

In Figure 4.19 are presented, for $c_1 t/L < 2.00$, the maximum values of the normalized mode I dynamic stress intensity factor, $\bar{K}_{I_{max}}$, computed using the four contours, along with $\bar{K}_{I_{max}}$ from the analytical solution. Values for $\bar{K}_{I_{max}}$ from the different contours varied by only 0.7%, with an average value of 1.09. By comparison, $\bar{K}_{I_{max}}$ was 1.17 in the analytical solution and the $J_{rg}(t)$-integral produced results which are lower than the analytical solution by 7%. Also plotted in Figure 4.19 are $\bar{K}_{I_{max}}$ computed by neglecting the material inertia term in equation (2.32). In this case only the static† version of $J_{rg}(t)$ was employed, differing from that given in references [5-7] by the integral over Γ_s in $J_{rg}(t)$. The result was a loss of path independence such that errors in $\bar{K}_{I_{max}}$ ranged between 12 - 17%. Then the $\bar{K}_{I_{max}}$ was generally less than unity.

4.2.2 Case 5: A Thick-Walled Cylinder Containing an Inner-Circumferential Edge Crack, Subjected to Sudden End Loadings

This case represents the class of transient crack problems in which an incident stress wave is diffracted by a crack. No existing solution is known to the author. Hence, the linear extrapolation technique [14] was employed to

---

† The material's inertia effects were still included in the finite element field solution to the problem.

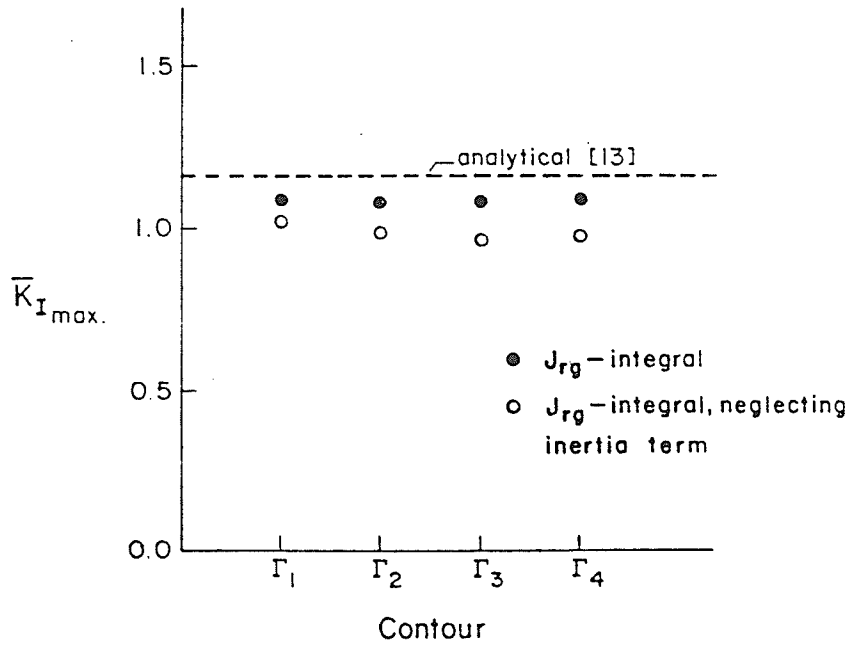

Figure 4.19 - Maximum values of $\bar{K}_I(t)$ for non-dimensionalized times, $c_1 t/L$, < 2.0 , for the cracked solid cylinder.

compare with the results from the $J_{rg}(t)$-integral. This technique was chosen to minimize the required programming.

A hollow circular cylinder of inner radius r_1, outer radius r_2 and length $2L$ is illustrated in Figure 4.20. The cylinder contains an axisymmetric inner-edge crack of zero thickness and tip radius a. The shape of the cylinder is given by $r_1/r_2 = 0.30$ and $(r_2 - r_1)/L = 0.75$, with $(a - r_1)/(r_2 - r_1) = 0.40$. Poisson's ratio is 0.29. The ends of the cylinder, at $z = \pm L$, were subjected to a uniform tensile stress σ_o which followed a unit Heaviside step-function time dependence.

4.2.2a Application of the $J_{rg}(t)$-Integral

Due to symmetry, only the upper-half of the problem was modelled numerically. As the crack was unpressurized, the integral over r_s in equation (2.32) was zero. The finite element grid is illustrated in Figure 4.21. The mesh consists of 300 uniform square elements with 336 nodes. As in Case 4, the mesh size is very coarse relative to the theoretically high stress gradients near the crack tip, with an element size equal to $(a - r_1)/6$. Computations were performed by using the four contours illustrated by the dashed lines in Figure 4.21.

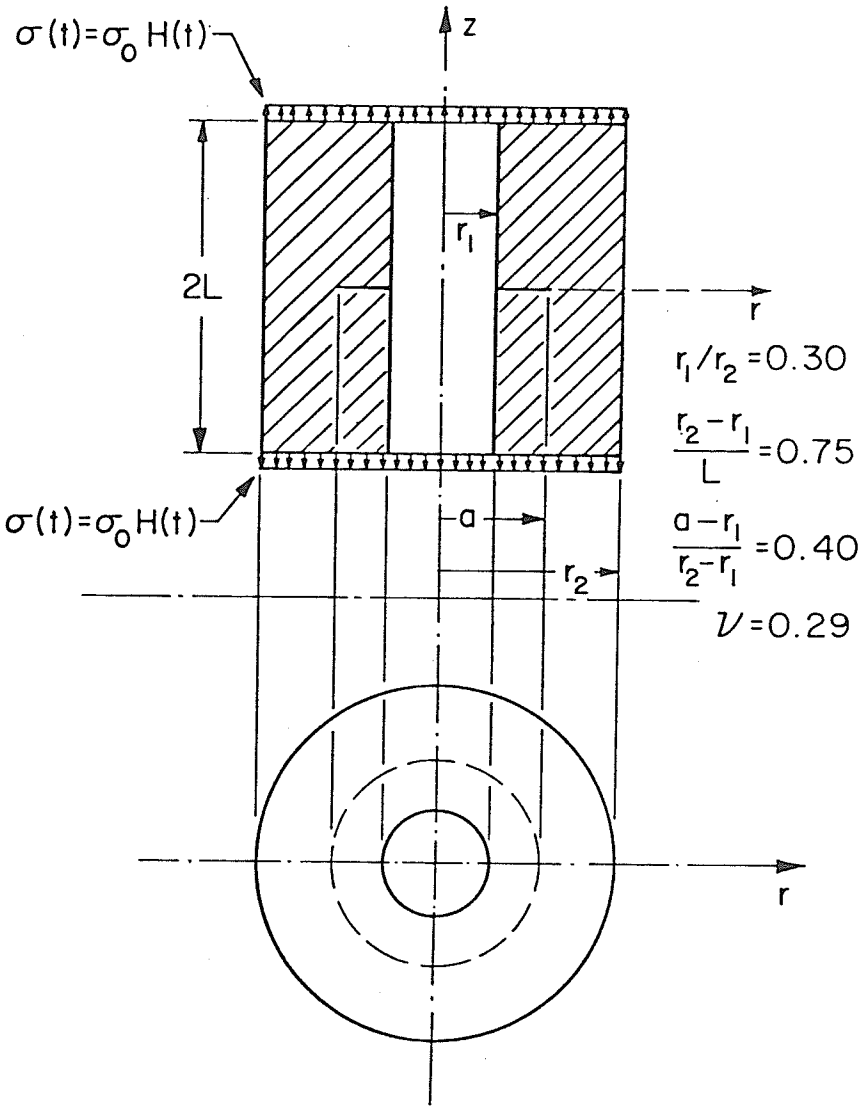

Figure 4.20 - A thick-walled circular cylinder with an inner-circumferential edge crack.

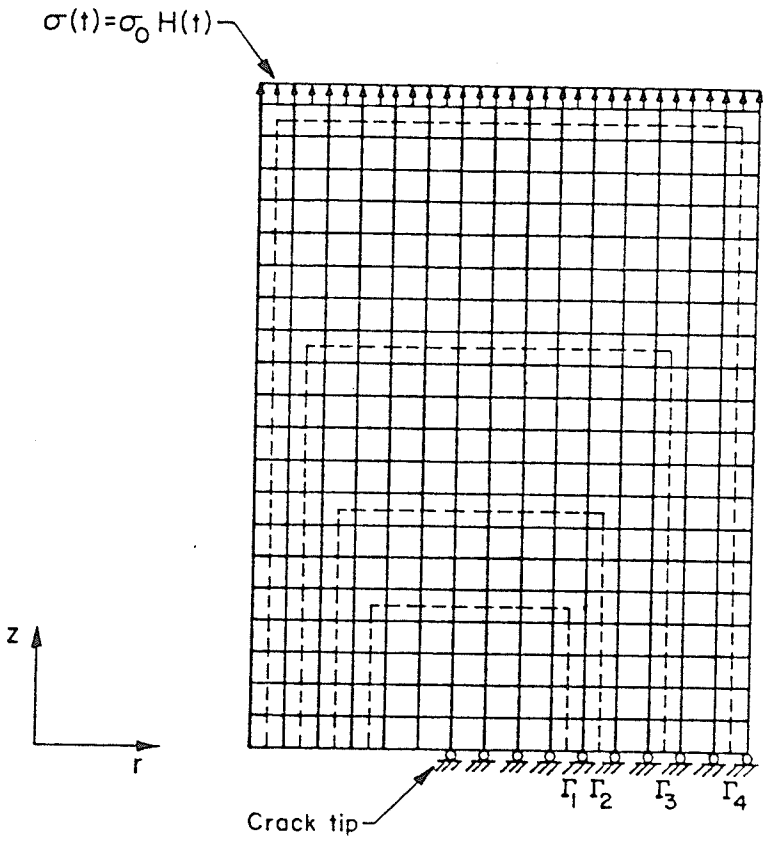

Figure 4.21 - Finite element model of the cracked thick-walled cylinder used in the $J_{rg}(t)$-integral computations, with contours as illustrated.

4.2.2b Application of the Linear Extrapolation Technique

In using the linear extrapolation technique, equation (1.1), which is applicable to axisymmetric cracks, was written to express $K_I(t)$ as a function of $\sigma_{zz}(R,\phi,t)$ along $\phi = 0$. (See Figure 1.1). At a given time, values of parameter $K_I'(R,t)$ were obtained at several positions along R from the $\sigma_{zz}(R,0,t)$ computed at these same positions by using the conventional elastodynamic TEPSAD code. A line was fitted to these values, as illustrated in Figure 4.24, by employing the least squares curve-fitting technique [56]. This line was extrapolated to the crack tip to determine $K_I(t)$, where $K_I(t) = K_I'(0,t)$. Details are given in Appendix VI where it is demonstrated that a truncation error in the extrapolated value for $K_I(t)$ is $\mathbf{0}((R/a)^2)$.

The finite element mesh used in the linear extrapolation technique is presented in Figures 4.22a and 4.22b. A non-uniform grid of 377 elements and 375 nodes was used. The size of the elements in the region of the crack tip is equal to $(a - r_1)/30$. Consequently, the stress singularity, which is a crucial requirement of this technique, is modelled effectively. The size of the time-step was governed by these small elements and the computations required five times the number of time-steps as compared with the $J_{rg}(t)$-integral analysis. As the finite element discretization error in modelling the stress singularity

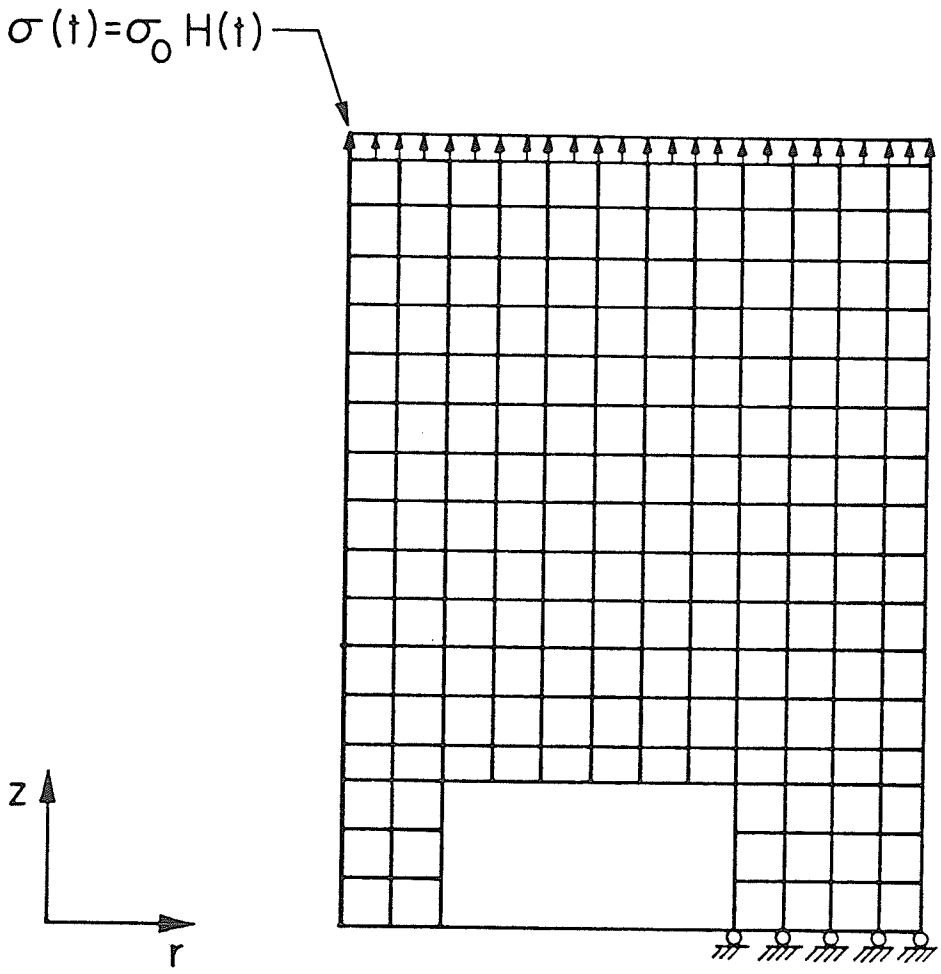

Figure 4.22a - Finite element model of the cracked thick-walled cylinder used in the linear extrapolation technique, excluding crack-tip details.

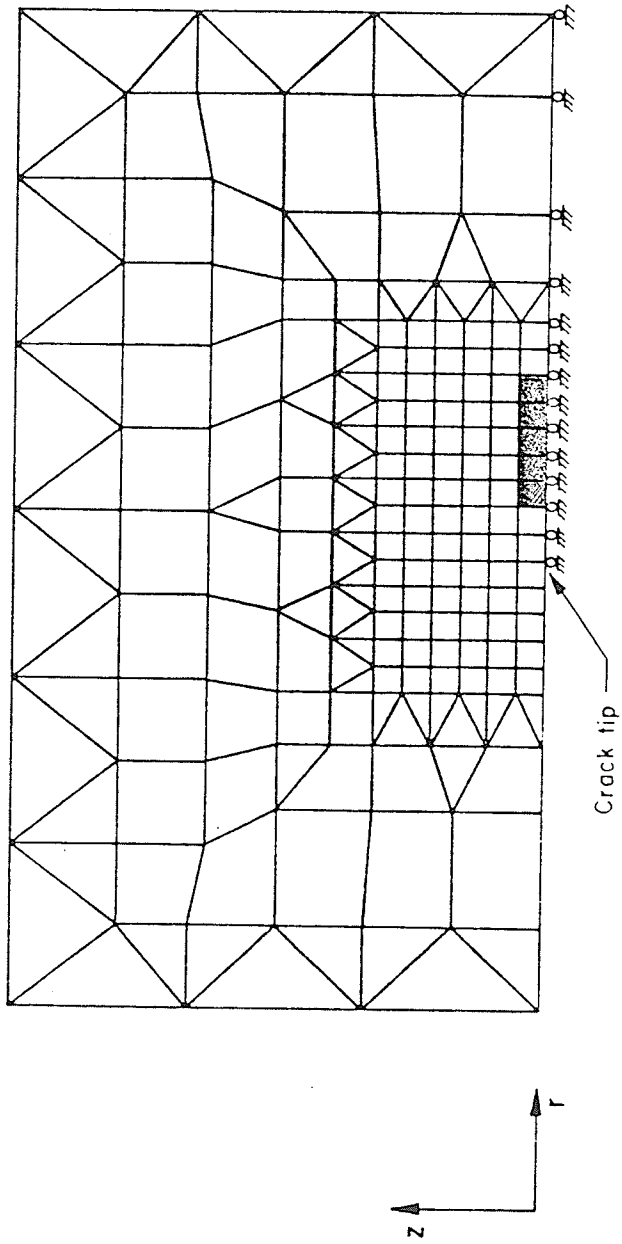

Figure 4.22b - Crack-tip details of the finite element model of the thick-walled cylinder used in the linear extrapolation technique.

increases as R decreases, the two elements closest to the crack tip were not utilized in the extrapolation. As well, only the five following elements, shown shaded in Figure 4.22b, were employed to minimize the linear extrapolation truncation error, where $0.007 < (R/a)^2 < 0.049$ for these elements.

4.2.2c Results and Discussion

Values of shear stress (not shown) were small relative to the normal stresses, as in Case 2. Thus, the approximation of this case as a mode I fracture condition is valid. In Figures 4.23a and 4.23b are shown $\bar{K}_I(t)$ at various non-dimensionalized times, $c_1 t/L$, computed by using the four contours. The static stress intensity factor, K_{I_s}, was found in reference [2] to be $0.913\sigma_o\sqrt{\pi a}$. These figures indicate that the $J_{rg}(t)$-integral is approximately path independent in wave diffraction problems during the increase (Figure 4.23a) and decrease (Figure 4.23b) in $\bar{K}_I(t)$. An exception to this general result occurred at $c_1 t/L = 4.50$, at which time values for $\bar{K}_I(t)$ computed by using r_3 and r_4 differed by 28%. As in Case 4, these errors are attributed to the discretization of the problem.

Presented in Figure 4.24 are the normalized values $\bar{K}_I'(R,t)$ against R/a at the non-dimensionalized time at

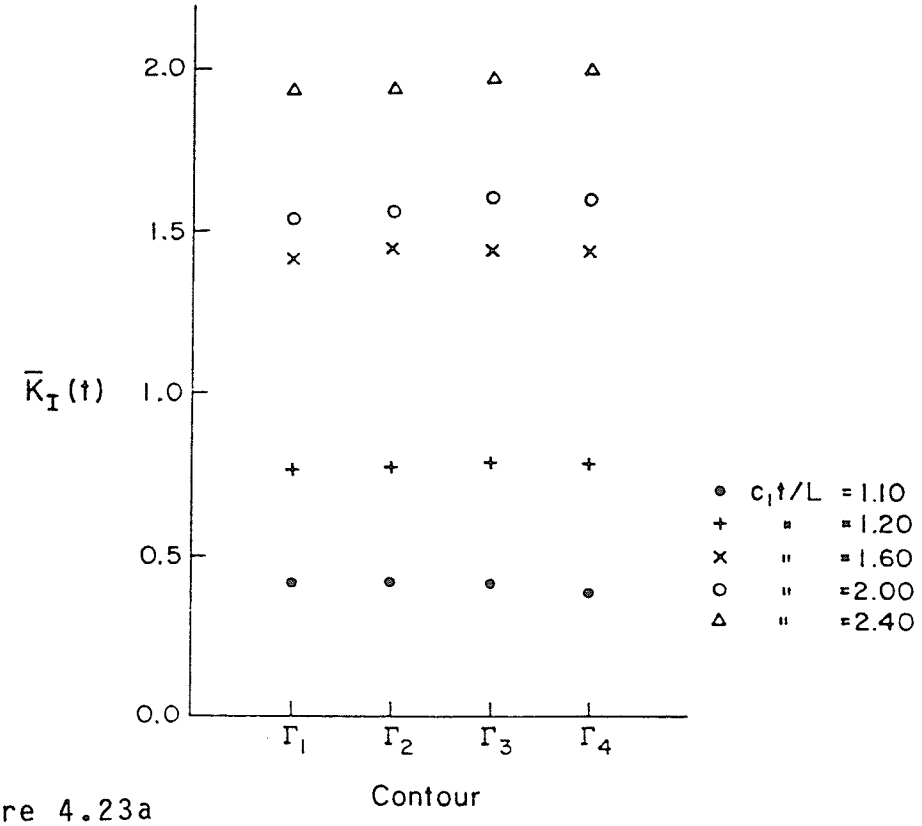

Figure 4.23a

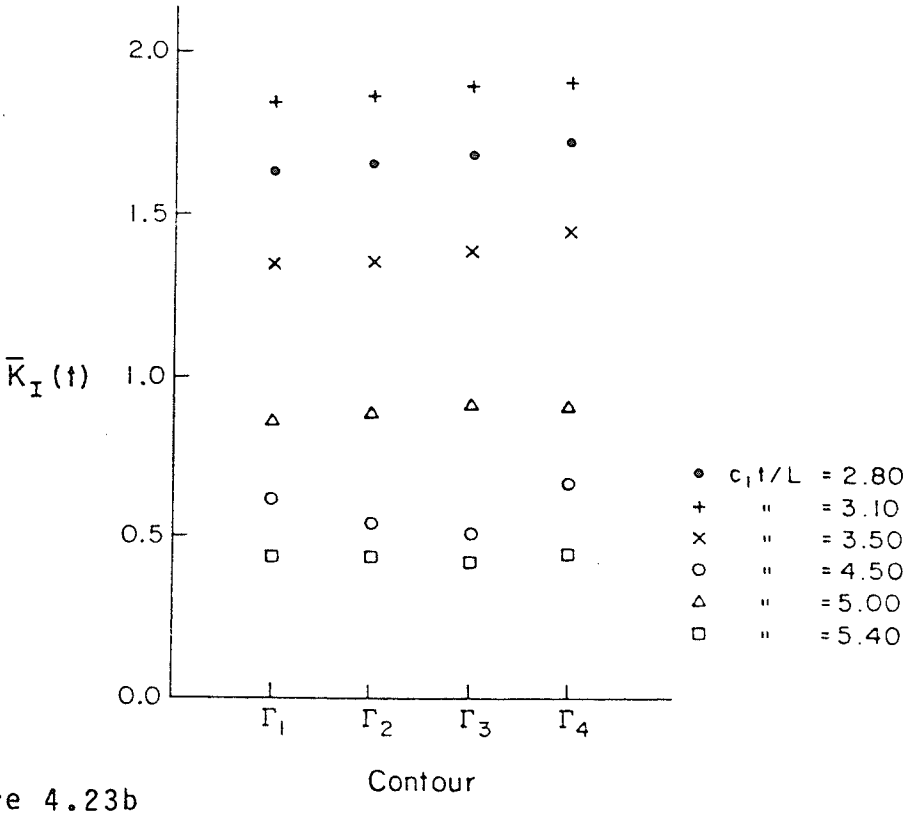

Figure 4.23b

Figures 4.23a - 4.23b Illustration of the path independence of the $J_{rg}(t)$-integral computation of $\bar{K}_I(t)$ for the cracked thick-walled cylinder.

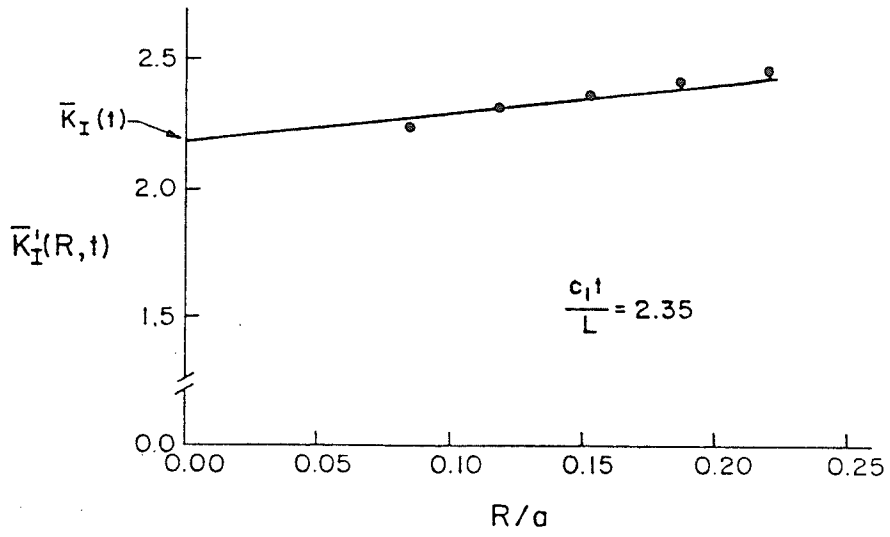

Figure 4.24 - Illustration of obtaining $\bar{K}_I(t)$ by using the linear extrapolation technique.

which $\bar{K}_I(t)$ was a maximum. Normalization was performed by using equation (4.1). It is reasonable to assume that the discretization error in the furthest shaded element was low. Thus, since the plotted points are similar in configuration to those presented in [14], it was concluded that the linear extrapolation technique would yield reasonably accurate values for $\bar{K}_I(t)$.

In Figure 4.25 is presented the non-dimensionalized time history of $\bar{K}_I(t)$ computed by means of the $J_{rg}(t)$-integral using the contour Γ_2[†] and the linear extrapolation technique. In elastodynamic crack analyses the quantity generally required for practical purposes is the maximum value of $K_I(t)$. Thus, the analysis did not proceed to the times corresponding to $\bar{K}_I(t)$ oscillating about the static equilibrium value of $\bar{K}_I(t) = 1.0$.

The close agreement between the two solutions is typified by $J_{rg}(t)$ having produced values generally lower than those from the linear extrapolation technique. This may be a consequence of the relatively coarse elements used in the $J_{rg}(t)$-integral analysis. The two curves have the same form as those resulting from a similar problem under plane strain conditions [14,19,23,24]. As was found in the previous cases, the TEPSAD code propagated the dilatational wave at a velocity higher than the theoretical c_1 . The incident wave arrived at $c_1 t/L = 0.9$, denoted as η_1 in Figure 4.25, rather than the

[†] Similar plots would be obtained from the other contours.

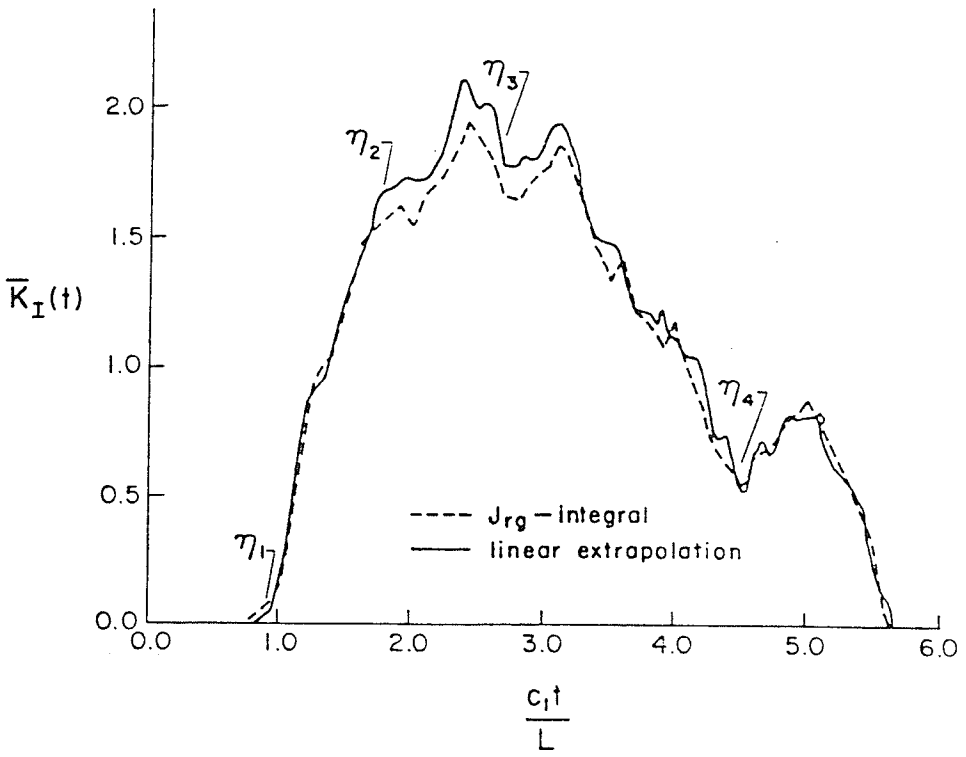

Figure 4.25 - Variation of $\bar{K}_I(t)$ with non-dimensionalized time for the cracked thick-walled cylinder.

theoretical time of $c_1 t/L = 1.0$. Other wavefront arrival times, based on the TEPSAD generated wave speed, are shown. The interval $(\eta_2 - \eta_1)$ was the time required for the tension wave generated at the crack tip to reflect from the free boundary at $r = r_2$ and return to the crack tip as a compression wave reducing the rate of increase in $\bar{K}_I(t)$. The time $(\eta_3 - \eta_1)$ was that needed for the incident dilatational wave, having just been reflected at $z = 0$, to travel back to the free end at $z = L$, reflect off the free end and return to the crack. Similarly, $(\eta_4 - \eta_3)$ was the time required for this latter wavefront to return to the free end at $z = L$ and travel back to the crack to reinforce the existing tensile stresses.

In Figure 4.26 are shown values of $\bar{K}_{I_{max}}$ computed by using the four $J_{rg}(t)$-integral contours and the linear extrapolation technique. The largest variation in $\bar{K}_{I_{max}}$ between any two contours was 3.6% , with an average value for $\bar{K}_{I_{max}}$ of 1.97 . The linear extrapolation method produced a $\bar{K}_{I_{max}}$ of 2.11 and the values from using $J_{rg}(t)$ were lower by 8.1 to 4.7% of this value for r_1 to r_4 , respectively. Also shown are $\bar{K}_{I_{max}}$ computed by neglecting the inertia term in equation (2.32). As in Case 4, there was an increase in path dependence and the differences in $\bar{K}_{I_{max}}$ with that from the linear extrapolation technique increased to 19 to 15% for r_1 to r_4 , respectively.

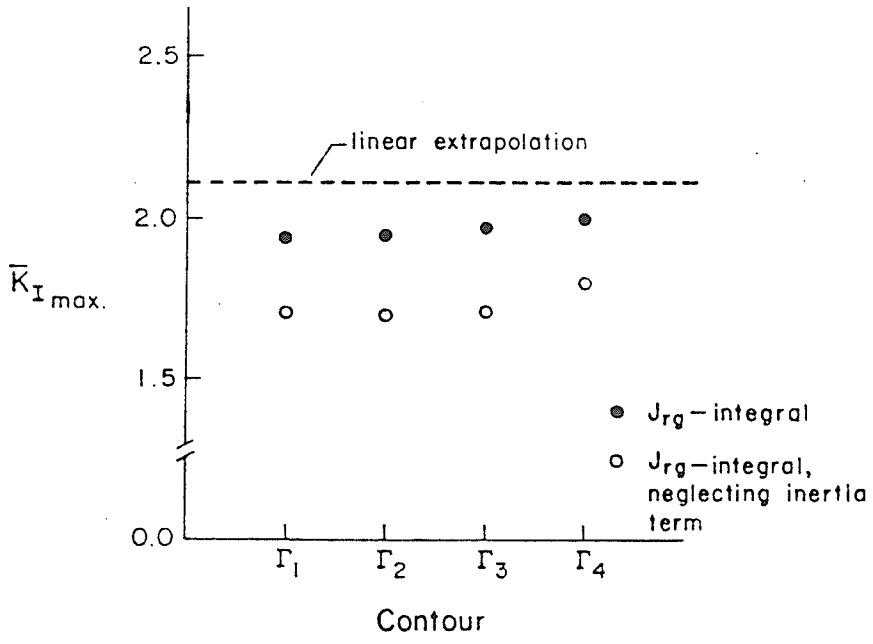

Figure 4.26 - Maximum values of $\bar{K}_I(t)$ for the cracked thick-walled cylinder.

CHAPTER FIVE

CONCLUSIONS AND RECOMMENDATIONS

A useful technique has been developed for obtaining approximate solutions to the dynamic stress intensity factor for stationary cracks under axisymmetric mode I conditions. This technique is based on the computation of a path-independent integral, $J_{rg}(t)$, which was formulated to describe the energy flux to the crack tip for a general class of axisymmetric mode I conditions. This integral was developed by equating the rates of work done by various forces in a solid.

An existing finite element computer code, TEPSA, was extended to simulate wave propagation in linear elastic solids. Ensuing results were validated by comparison with other solutions. The finite element code served as a computational tool to evaluate the $J_{rg}(t)$-integral.

Numerical values of $\bar{K}_I(t)$ computed by using $J_{rg}(t)$ were approximately path independent and values of $\bar{K}_{I_{max}}$ were in good agreement with other solutions. Contributions from the material inertia term in the $J_{rg}(t)$-integral were approximately an order of magnitude smaller than the total values of $J_{rg}(t)$. Thus, this term may be neglected if the relative uncertainty in the loading falls substantially

outside this range. The results showed that the $J_{rg}(t)$-integral does not require a detailed numerical field solution near the crack tip. Thus, this technique is convenient and economical to use. Practical applications include approximate solutions, or bounds, to problems involving thick-walled pipes and pressure vessels containing a partially-through crack around a portion of the circumference, subjected to a shock loading.

Further research should test the $J_{rg}(t)$-integral in cases involving edge cracks and problems where the effects of thermal strains and plastic strains are significant. As well, the formulations presented in this thesis should be regarded as an intermediate step in the development of a more general path-independent energy-flux integral. Such an integral would accommodate the three-dimensional analysis of non-axisymmetric circumferential cracks in cylindrical structures subjected to general loading conditions. The $J_{rg}(t)$-integral must be extended, following the concepts presented here, to account for such cases and augment the pragmatic value of this technique.

REFERENCES

1. Chen, E. P. and Sih, G. C. "Transient response of cracks to impact loads", In Sih, G. C. Editor "Mechanics of Fracture 4 Elastodynamic Crack Problems", Noordhoff International (1977) 1-58.

2. Erdol, R. and Erdogan, F. "A thick-walled cylinder with an axisymmetric internal or edge crack", Transactions of the ASME, Journal of Applied Mechanics 45 (1978) 281-286.

3. Atsumi, A. and Shindo, Y. "Singular stresses in a transversely isotropic circular cylinder with circumferential edge crack", International Journal of Engineering Science 17 (1979) 1229-1236.

4. Emery, A. F., Cupps, F. J. and Neighbors, P. K. "The use of singularity programming in finite element calculations of elastic stress intensity factors, plane and axisymmetric-applied to thermal stress fracture", In "Computational Fracture Mechanics", ASME 2nd National Congress on Pressure Vessels and Piping, San Francisco, Calf., (June 23-27, 1975) 35-48.

5. Bergkvist, H. and Huong, G. L. "J-integral related quantities in axisymmetric cases", International Journal of Fracture 13 (1977) 556-558.

6. Astiz, M. A., Elices, M. and Sánchez-Gálves, V. Discussion: "J-integral related quantities in axisymmetric cases", by Bergkvist, H. and Huong, G. L., International Journal of Fracture 14 (1978) R39-R40.

7. Bergkvist, H. and Huong, G. L. ICF4 Response: Discussion of "J-integral related quantities in axisymmetric cases", by Astiz, M. A., Elices, M. and Sánchez-Gálves, V., International Journal of Fracture 14 (1978) R85-R86.

8. Astiz, M. A., Elices, M. and Sánchez-Gálves, V. "On the singular behaviour of the stress distribution near a crack tip in axisymmetric problems and hardening materials", International Journal of Fracture 16 (1980) R191-R193.

9. Kanninen, M. F. "A critical appraisal of solution techniques in dynamic fracture mechanics", In "Proceedings of the 1st International Conference on Numerical Methods in Fracture Mechanics", University College of Swansea (Jan., 1978) 612-633.

10. Thau, S. A. and Lu, T. "Transient stress intensity factors for a finite crack in an elastic solid caused by a dilatational wave", International Journal of Solids and Structures 7 (1971) 731-750.

11. Chen, E. P. and Sih, G. C. "Scattering waves about stationary and moving cracks", in Sih, G. C. Editor "Mechanics of Fracture 4 Elastodynamic Crack Problems", Noordhoff International (1977) 119-212.

12. Achenbach, J. D., Keer, L. M. and Mendelsohn, D. A. "Elastodynamic analysis of an edge crack", Transactions of the ASME, Journal of Applied Mechanics 47 (1980) 551-556.

13. Chen, E. P. "Elastodynamic response of a penny-shaped crack in a cylinder of finite radius", International Journal of Engineering Science 17 (1979) 379-385.

14. Chen, Y. M. and Wilkins, M. L. "Numerical analysis of dynamic crack problems", In Sih, G. C. Editor "Mechanics of Fracture 4 Elastodynamic Crack Problems", Noordhoff International (1977) 295-345.

15. Kobayashi, A. S., Mall, S., Urabe, Y. and Emery, A. F. "A numerical dynamic fracture analysis of three wedge-loaded DCB specimens", In "Proceedings of the 1st International Conference on Numerical Methods in Fracture Mechanics", Univeristy College of Swansea (Jan., 1978) 673-684.

16. Mall, S., Kobayashi, A. S. and Urabe, Y. "Dynamic photoelastic and dynamic finite element analyses of dynamic-tear-test specimens", Experimental Mechanics 18 (1978) 449-455.

17. Aberson, J. A., Anderson, J. M. and King, W. W. "Dynamic analysis of cracked structures using singularity finite elements", In Sih, G. C. Editor "Mechanics of Fracture 4 Elastodynamic Crack Problems", Noordhoff International (1977) 249-294.

18. Bažant, Z. P., Glazik, Jr., J. L. and Achenbach, J. D. "Finite element analysis of wave diffraction by a crack", Transactions of the ASCE, Journal of Engineering Mechanics Division EM3 (1976) 479-496.

19. Aoki, S., Kishimoto, K., Kondo, H. and Sakata, M. "Elastodynamic analysis of crack by finite element method using singular element", International Journal of Fracture 14 (1978) 59-68.

20. Kelley, J. W. and Sun, C. T. "A singular finite element for computing time dependent stress intensity factors", Engineering Fracture Mechanics 12 (1979) 13-22.

21. Glazik, Jr., J. L. "Dynamic finite element analysis of cracked bodies", Transactions of the ASME, Journal of Pressure Vessel Technology 102 (1980) 2-7.

22. Mall, S. "Dynamic finite element analysis of cracked bodies with stationary crack", In Paris, P. C. Editor "Fracture Mechanics: Twelfth Conference", ASTM STP 700, American Society for Testing and Materials, Philadelphia (1980).

23. Mall, S. "A finite element analysis of transient crack problems with a path-independent integral", In "Advances in Fracture Research", 5th International Conference on Fracture, held in Cannes, France (March 29-April 3, 1981).

24. Kishimoto, K., Aoki, S. and Sakata, M. "Dynamic stress intensity factors using $\hat{J}$-integral and finite element method", Engineering Fracture Mechanics 13 (1980) 387-394.

25. Rolfe, S. T. and Barsom, J. M. "Fracture and Fatique Control in Structures", Prentice-Hall, Inc. (1977) 30-51.

26. Rice, J. R. "A path-independent integral and the approximate analysis of strain concentration by notches and cracks", Transactions of the ASME, Journal of Applied Mechanics (1968) 379-386.

27. Rice, J. R. "Mathematical analysis in the mechanics of fracture", In Liebowitz, H. Editor "Fracture - An Advanced Treatise II Mathematical Fundamentals", Academic Press (1968) 191-311.

28. Atkinson, C. and Eshelby, J. D. "The flow of energy into the tip of a moving crack", International Journal of Fracture Mechanics 4 (1968) 3-8.

29. Broberg, K. B. "Crack-growth criteria and non-linear fracture mechanics", Journal of the Mechanics and Physics of Solids 19 (1971) 407-418.

30. Freund, L. B. "Energy flux into the tip of an extending crack in an elastic solid", Journal of Elasticity 2 (1972) 341-349.

31. Nilsson, F. "A path-independent integral for transient crack problems", International Journal of Solids and Structures 9 (1973) 1107-1115.

32. Gurtin, M. E. "On a path-independent integral for elastodynamics", International Journal of Fracture 12 (1976) 643-644.

33. Bui, H. D. "Stress and crack-displacement intensity factor in elastodynamics", In Taplin, D. M. R. Editor "Advances in Research on the Strength and Fracture of Materials", Pergamon Press 3A (1977) 91-95.

34. Kishimoto, K., Aoki, S. and Sakata, M. "On the path-independent integral-$\hat{J}$", Engineering Fracture Mechanics 13 (1980) 841-850.

35. Barenblatt, G. I., Advances in Applied Mechanics 7 (1962).

36. Lai, W. M., Rubin, D. and Krempl, E. "Introduction to Continuum Mechanics", Revised Edition, Pergamon Press (1978).

37. Fung, Y. C. "Foundations of Solid Mechanics", Prentice-Hall, Inc. (1965).

38. Sih, G. C. "Dynamic aspects of crack propagation", In Kanninen, M. F. et al. Editors "Inelastic Behaviour of Solids", McGraw-Hill Co. (1969) 607-639.

39. Greenberg, M. D. "Foundations of Applied Mathematics", Prentice-Hall, Inc. (1978) 150-195.

40. Hsu, T. R., Bertels, A.W.M., Banerjee, S. and Harrison, W. C. "Theoretical basis for a transient thermal elastic-plastic stress analysis of nuclear reactor fuel elements", Atomic Energy of Canada Ltd., Pinawa AECL-5233 (1976).

41. Clough, R. W. "Analysis of structural vibrations and dynamic response", In Gallagher, R. H., Yamada, Y. and Oden, J. T. Editors "Recent Advances in Matrix Methods of Structural Analysis and Design", University of Alabama Press (1971).

42. Clough, R. W. "Finite element analysis of dynamic response", In Oden, J. T. et al. Editors "Advances in Computational Methods in Structural Mechanics and Design", Proceedings of the 2nd U.S.-Japan Seminar on Matrix Methods of Structural Analysis and Design, UAH Press, University of Alabama in Huntsville, Alabama (1972) 153-179.

43. Zienkiewicz, O. C. "The Finite Element Method in Engineering Science", 2nd Edition, McGraw-Hill (1971).

44. Clough, R. W. and Penzien, J. "Dynamics of Structures", McGraw-Hill (1975).

45. Bathe, K. and Wilson, E. L. "Numerical Methods in Finite Element Analysis", Prentice-Hall, Inc. (1976).

46. Newmark, N. M. "A method of computation for structural dynamics", Proceedings of the American Society of Civil Engineers 85 EM3 (1959) 67-94.

47. Verner, E. A. and Becker, E. B. "Finite element stress formulation for wave propagation", International Journal for Numerical Methods in Engineering 7 (1973) 441-459.

48. Biffle, J. H. "Finite Element Analysis for Wave Propagation in Elastic-Plastic Solids", Ph.D. Dissertation, Division of Engineering Mechanics, The University of Texas at Austin, Report 73-4 (1973).

49. Bathe, K. J. and Wilson, E. L. "Stability and accuracy analysis of direct integration methods", Earthquake Engineering and Structural Dynamics 1 (1973) 283-291.

50. Desai, C. S. and Abel, J. F. "Introduction to the Finite Element Method", Van Nostrand Reinhold Co. (1972).

51. Morse, P. M. and Feshbach, H. "Methods of Theoretical Physics", McGraw-Hill, Inc. (1953) 275-347.

52. Ghosh, S. and Wilson, E. "Dynamic Stress Analysis of Axisymmetric Structures under Arbitrary Loading", College of Engineering, University of California, Berkley, Calf., EERC 69-10 (1969).

53. Wilson, E. L., Bathe, K. and Doherty, W. P. "Direct solution of large systems of linear equations", Computers and Structures 4 (1974) 363-372.

54. Kolsky, H. "Stress Waves in Solids", Dover Publications, Inc. (1963).

55. Lakshminarayanan, V. "On the Development of a Refined Finite-Element Free From Discretization-Dispersion for Elastic Wave Propagation Modelling", Ph.D. Dissertation, Montana State University (1973).

56. Stanton, R. G. "Numerical Methods for Science and Engineering", Prentice-Hall, Inc. (1961) 52-62.

APPENDIX I

FORMULATION OF EQUATION (2.18)

The matrix components of ϵ in the cylindrical coordinate system [37] are, for the axisymmetric case,

$$\epsilon_{ij} = \begin{bmatrix} \frac{\partial u_r}{\partial r} & 0 & \frac{1}{2}\left(\frac{\partial u_z}{\partial r} + \frac{\partial u_r}{\partial z}\right) \\ 0 & \frac{u_r}{r} & 0 \\ \frac{1}{2}\left(\frac{\partial u_z}{\partial r} + \frac{\partial u_r}{\partial z}\right) & 0 & \frac{\partial u_z}{\partial z} \end{bmatrix} .$$

Differentiating ϵ_{ij} with respect to r and writing the resulting components as the sum of two matrices gives

$$\frac{\partial \epsilon_{ij}}{\partial r} = \begin{bmatrix} \frac{\partial^2 u_r}{\partial r^2} & 0 & \frac{1}{2}\left(\frac{\partial^2 u_r}{\partial r \partial z} + \frac{\partial^2 u_z}{\partial r^2}\right) \\ 0 & \frac{1}{r}\frac{\partial u_r}{\partial r} & 0 \\ \frac{1}{2}\left(\frac{\partial^2 u_z}{\partial r^2} + \frac{\partial^2 u_r}{\partial r \partial z}\right) & 0 & \frac{\partial^2 u_z}{\partial r \partial z} \end{bmatrix}$$

$$+ \begin{bmatrix} 0 & 0 & 0 \\ 0 & \frac{-u_r}{r^2} & 0 \\ 0 & 0 & 0 \end{bmatrix} . \qquad \text{(A1)}$$

By following the example derivation presented in reference [36] for the gradient $\nabla \mathbf{u}$ in polar coordinates, it can be shown that the matrix components of $\nabla(\partial \mathbf{u}/\partial r)$ in cylindrical coordinates for the axisymmetric case are

$$\left(\nabla \frac{\partial \mathbf{u}}{\partial r}\right)_{ij} = \begin{bmatrix} \frac{\partial^2 u_r}{\partial r^2} & 0 & \frac{\partial^2 u_r}{\partial z \partial r} \\ 0 & \frac{1}{r}\frac{\partial u_r}{\partial r} & 0 \\ \frac{\partial^2 u_z}{\partial r^2} & 0 & \frac{\partial^2 u_z}{\partial z \partial r} \end{bmatrix} . \qquad \text{(A2)}$$

Upon comparing equations (A1) and (A2), one may write

$$\frac{\partial \varepsilon_{ij}}{\partial r} = \frac{1}{2}\left(\left(\nabla \frac{\partial \mathbf{u}}{\partial r}\right)_{ij} + \left(\nabla \frac{\partial \mathbf{u}}{\partial r}\right)_{ji}\right) + H_{ij} \quad , \qquad \text{(A3)}$$

where H_{ij} is the second matrix in equation (A1).

Upon taking the product of equation (A3) with σ_{ij} and rearranging, one obtains

$$\frac{1}{2}\left(\sigma_{ij}\left(\nabla \frac{\partial \mathbf{u}}{\partial r}\right)_{ij} + \sigma_{ij}\left(\nabla \frac{\partial \mathbf{u}}{\partial r}\right)_{ji}\right) = \sigma_{ij}\frac{\partial \varepsilon_{ij}}{\partial r} + \frac{\sigma_{\theta\theta}\varepsilon_{\theta\theta}}{r} \quad , \qquad \text{(A4)}$$

because $\varepsilon_{\theta\theta} = u_r/r$. Since the stress tensor is symmetric,

$$\sigma_{ij}\left(\nabla \frac{\partial \mathbf{u}}{\partial r}\right)_{ji} = \sigma_{ji}\left(\nabla \frac{\partial \mathbf{u}}{\partial r}\right)_{ji} = \sigma_{ij}\left(\nabla \frac{\partial \mathbf{u}}{\partial r}\right)_{ij} \quad , \qquad \text{(A5)}$$

as i,j are dummy indicies. Therefore, by substituting equation (A5) into (A4), one has

$$\sigma_{ij}\left(\nabla \frac{\partial \mathbf{u}}{\partial r}\right)_{ij} = \sigma_{ij}\frac{\partial \varepsilon_{ij}}{\partial r} + \frac{\sigma_{\theta\theta}\varepsilon_{\theta\theta}}{r} \quad .$$

APPENDIX II

PARTIAL DERIVATIVE OF ELASTIC STRAIN ENERGY DENSITY FUNCTION WITH RESPECT TO r

The elastic strain energy density function is defined by [37],

$$\frac{\partial W}{\partial \varepsilon^{e}_{ij}} = \sigma_{ij} \quad . \tag{A6}$$

The W is not an explicit function of r so that the partial derivative of W with respect to r can be expressed using the chain rule as

$$\frac{\partial W}{\partial r} = \frac{\partial W}{\partial \varepsilon^{e}_{ij}} \frac{\partial \varepsilon^{e}_{ij}}{\partial r} \quad . \tag{A7}$$

By substituting equation (A6) into (A7), one has

$$\frac{\partial W}{\partial r} = \sigma_{ij} \frac{\partial \varepsilon^{e}_{ij}}{\partial r} \quad .$$

APPENDIX III

INTEGRATION OF $\int_A \frac{\partial W}{\partial r} \frac{r}{a} dA$ BY PARTS

Consider the convex region illustrated in Figure A1. The line functions $f_L(z)$ and $f_R(z)$ constitute Γ and form the left- and right-hand boundaries, respectively, for any horizontal line passing through A .

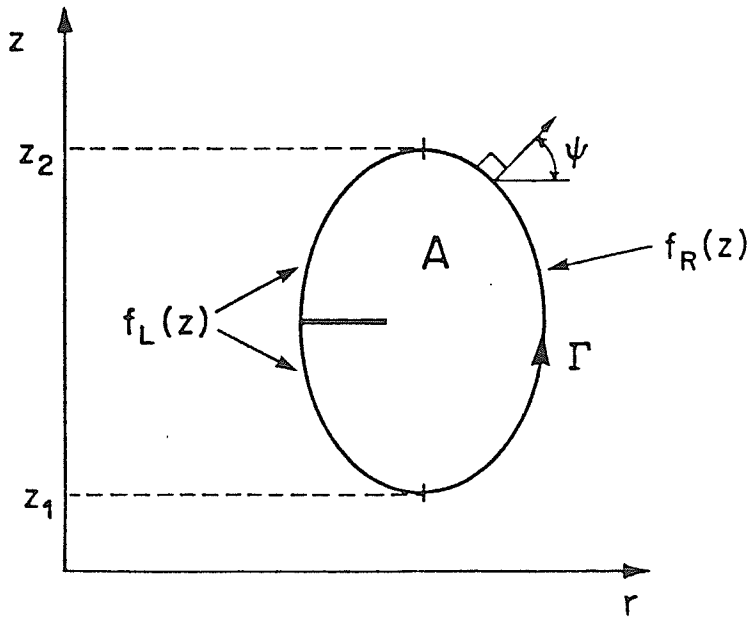

Figure A1 - Region of integration.

To integrate

$$I_3 = \int_A \frac{\partial W}{\partial r} \frac{r}{a} dA \quad ,$$

make the substitution

$$dA = drdz$$

such that

$$I_3 = \int_{z_1}^{z_2} \int_{f_L(z)}^{f_R(z)} \frac{\partial W}{\partial r} \frac{r}{a} \, dr dz \quad . \tag{A8}$$

In equation (A8) it is assumed that the crack has zero width in the r-z plane. Integrate equation (A8) by parts to give

$$I_3 = \int_{z_1}^{z_2} \left(\frac{Wr}{a}\right)\Big|_{f_R(z)} dz - \int_{z_1}^{z_2} \left(\frac{Wr}{a}\right)\Big|_{f_L(z)} dz - \int_A \frac{W}{a} \, dA \quad ,$$

$$= \int_{z_1}^{z_2} \left(\frac{Wr}{a}\right)\Big|_{f_R(z)} dz + \int_{z_2}^{z_1} \left(\frac{Wr}{a}\right)\Big|_{f_L(z)} dz - \int_A \frac{W}{a} \, dA \quad .$$

In the first two integrals change the variable of integration to Γ using

$$dz = d\Gamma \cos\psi \quad ,$$

to arrive at

$$I_3 = \int_\Gamma W \cos(\psi) \frac{r}{a} \, d\Gamma - \int_A \frac{W}{a} \, dA \quad .$$

Note that although the region was assumed for simplicity to be convex, the integration can be extended to non-convex regions as well [39].

APPENDIX IV

EXPRESSION OF EQUATION (2.27) IN TERMS OF STRESS TENSOR COMPONENTS

The integrand of

$$I_2 = \int_{\Gamma + \Gamma_s} T_{n_i} \frac{\partial u_i}{\partial r} \frac{r}{a} \, d\Gamma \qquad (A9)$$

will be evaluated separately over Γ and Γ_s.

ON Γ

The matrix components of σ_{ij} in the cylindrical coordinate system are, in the axisymmetric case,

$$\sigma_{ij} = \begin{bmatrix} \sigma_{rr} & 0 & \sigma_{rz} \\ 0 & \sigma_{\theta\theta} & 0 \\ \sigma_{zr} & 0 & \sigma_{zz} \end{bmatrix} .$$

Those of n_j are (see Figure 2.1)

$$n_j = \begin{Bmatrix} \cos\psi \\ 0 \\ \sin\psi \end{Bmatrix} .$$

The components of T_{n_i} may now be found by performing the transformation given by equation (2.11).

$$T_{n_i} = \sigma_{ij} \, n_j = \begin{Bmatrix} \sigma_{rr}\cos\psi + \sigma_{rz}\sin\psi \\ 0 \\ \sigma_{zr}\cos\psi + \sigma_{zz}\sin\psi \end{Bmatrix}$$

The components of the vector $\partial u_i / \partial r$ are in the axisymmetric case

$$\frac{\partial u_i}{\partial r} = \begin{Bmatrix} \frac{\partial u_r}{\partial r} \\ 0 \\ \frac{\partial u_z}{\partial r} \end{Bmatrix} . \qquad \text{(A10)}$$

By evaluating the scalar product one has

$$T_{n_i} \frac{\partial u_i}{\partial r} = (\sigma_{rr} \frac{\partial u_r}{\partial r} + \sigma_{rz} \frac{\partial u_z}{\partial r})\cos\psi + (\sigma_{rz} \frac{\partial u_r}{\partial r} + \sigma_{zz} \frac{\partial u_z}{\partial r})\sin\psi \quad , \qquad \text{(A11)}$$

as $\sigma_{rz} = \sigma_{zr}$.

ON r_s

In mode I analyses crack-surface tractions are restricted to a normal pressure P and the components of σ_{ij} reduce to

$$\sigma_{ij} = \begin{bmatrix} 0 & 0 & 0 \\ 0 & 0 & 0 \\ 0 & 0 & -P \end{bmatrix} .$$

On the lower and upper crack faces $n_j = (0,0,+1)$ and $(0,0,-1)$, respectively, and n_j may be conveniently represented as

$$n_j = \begin{Bmatrix} 0 \\ 0 \\ \sin\psi \end{Bmatrix} .$$

Upon performing the transformation given by equation (2.11) one has

$$T_{n_i} = \begin{Bmatrix} 0 \\ 0 \\ -P \sin\psi \end{Bmatrix} .$$

From equation (A10) one may write the scalar product

$$T_{n_i} \frac{\partial u_i}{\partial r} = -P \frac{\partial u_z}{\partial r} \sin\psi \quad . \tag{A12}$$

Finally, substitute equations (A11) and (A12) into (A9) to obtain

$$I_2 = \int_\Gamma \left((\sigma_{rr} \frac{\partial u_r}{\partial r} + \sigma_{rz} \frac{\partial u_z}{\partial r}) \cos\psi + (\sigma_{rz} \frac{\partial u_r}{\partial r} + \sigma_{zz} \frac{\partial u_z}{\partial r}) \sin\psi \right) \frac{r}{a} \, d\Gamma$$

$$- \int_{\Gamma_s} P \frac{\partial u_z}{\partial r} \sin(\psi) \frac{r}{a} \, d\Gamma \quad .$$

APPENDIX V

FINITE ELEMENT LUMPED-MASS MATRIX

Axisymmetric Toroidal Element

Divide the element's cross-section into regions of equal area as illustrated below.

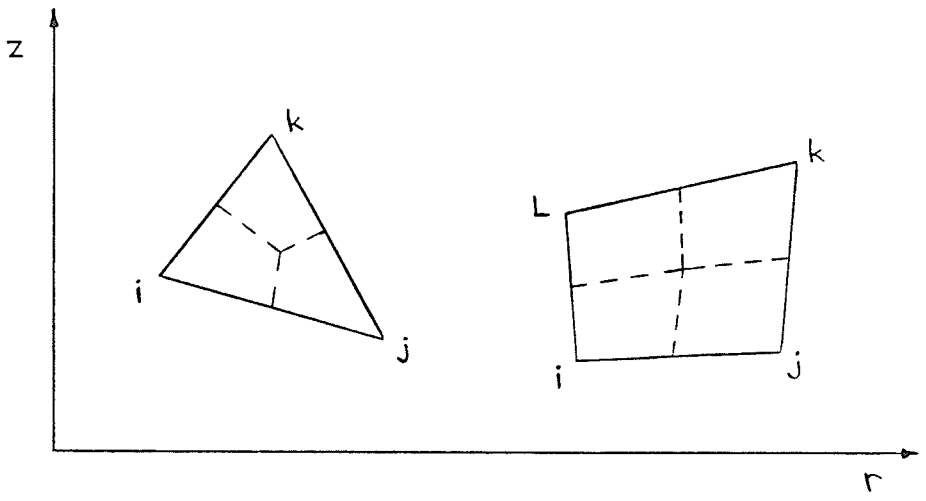

Figure A2 - Division of element in forming the lumped-mass matrix.

The mass allocated to each node is proportional to the centroidal radius of the adjacent region. Thus, for the triangular element the element mass matrix is given by

$$[M^e] = \frac{\rho V^e}{3 r_c} \begin{bmatrix} r_{c_i} & 0 & 0 & 0 & 0 & 0 \\ 0 & r_{c_i} & 0 & 0 & 0 & 0 \\ 0 & 0 & r_{c_j} & 0 & 0 & 0 \\ 0 & 0 & 0 & r_{c_j} & 0 & 0 \\ 0 & 0 & 0 & 0 & r_{c_k} & 0 \\ 0 & 0 & 0 & 0 & 0 & r_{c_k} \end{bmatrix},$$

where

$$r_c = \frac{(r_i + r_j + r_k)}{3}$$

and

$$r_{c_i} = \frac{1}{4}\left(2r_i + r_c + \frac{(r_j + r_k)}{2}\right)$$

$$r_{c_j} = \frac{1}{4}\left(2r_j + r_c + \frac{(r_i + r_k)}{2}\right)$$

$$r_{c_k} = \frac{1}{4}\left(2r_k + r_c + \frac{(r_i + r_j)}{2}\right) .$$

Similarly for a quadrilateral element one has

$$[M^e] = \frac{\rho V^e}{4 r_c}\begin{bmatrix} r_{c_i} & 0 & 0 & 0 & 0 & 0 & 0 & 0 \\ 0 & r_{c_i} & 0 & 0 & 0 & 0 & 0 & 0 \\ 0 & 0 & r_{c_j} & 0 & 0 & 0 & 0 & 0 \\ 0 & 0 & 0 & r_{c_j} & 0 & 0 & 0 & 0 \\ 0 & 0 & 0 & 0 & r_{c_k} & 0 & 0 & 0 \\ 0 & 0 & 0 & 0 & 0 & r_{c_k} & 0 & 0 \\ 0 & 0 & 0 & 0 & 0 & 0 & r_{c_l} & 0 \\ 0 & 0 & 0 & 0 & 0 & 0 & 0 & r_{c_l} \end{bmatrix} ,$$

where

$$r_c = \frac{(r_i + r_j + r_k + r_l)}{4}$$

and

$$r_{c_i} = \frac{1}{4}\left(2r_i + r_c + \frac{(r_j + r_l)}{2}\right)$$

$$r_{c_j} = \frac{1}{4}\left(2r_j + r_c + \frac{(r_i + r_k)}{2}\right)$$

$$r_{c_k} = \frac{1}{4}\left(2r_k + r_c + \frac{(r_j + r_l)}{2}\right)$$

$$r_{c_l} = \frac{1}{4}\left(2r_l + r_c + \frac{(r_i + r_k)}{2}\right) .$$

Plane Strain Element

In this case the element's mass is simply divided evenly among the nodes. Therefore, for a triangular element

$$[M^e] = \frac{\rho V^e}{3} [I]_{6x6}$$

and for a quadrilateral element

$$[M^e] = \frac{\rho V^e}{4} [I]_{8x8} ,$$

where $[I]$ is the identity matrix.

APPENDIX VI

CALCULATION OF $K_I(t)$ BY THE LINEAR EXTRAPOLATION TECHNIQUE

(from ref. [14], Appendix)

Equation (1.1) can be expanded for the stress component σ_{zz} in the neighbourhood of a crack tip, where $R \ll a$, in an infinite elastic medium at a given time, say t_1, as

$$\sigma_{zz}(R,\phi,t_1) = K_I(t_1)f_{-1/2}(\phi)R^{-1/2} + f_0(\phi,t_1) + f_{1/2}(\phi,t_1)R^{1/2} + f_1(\phi,t_1)R + f_{3/2}(\phi,t_1)R^{3/2} + f_2(\phi,t_1)R^2 + \mathbf{0}(R^{5/2}) \quad . \tag{A13}$$

In this expression

$$f_{-1/2}(\phi) = \cos(\tfrac{\phi}{2})(1 + \sin(\tfrac{\phi}{2})\sin(\tfrac{3\phi}{2})) \quad ,$$

$$\neq 0 \text{ for } 0 \leq |\phi| < \pi \quad ,$$

and $f_{n/2}(\phi,t_1)$ $(n = 0,1,2, \ldots)$ are functions of ϕ and t_1 with

$$f_{n/2}(0,t_1) = 0 \quad \text{for} \quad n = 0,2,4, \ldots \quad . \tag{A14}$$

Upon rearranging equation (A13) one obtains

$$K_I(t_1) = \frac{\sigma_{zz}(R,\phi,t_1)R^{1/2}}{f_{-1/2}(\phi)} - \frac{f_{1/2}(\phi,t_1)R}{f_{-1/2}(\phi)} - \frac{1}{f_{-1/2}(\phi)}\left(f_0(\phi,t_1)R^{1/2} + f_1(\phi,t_1)R^{3/2} + f_{3/2}(\phi,t_1)R^2 + f_2(\phi,t_1)R^{5/2} + \mathbf{0}(R^3)\right) \quad . \tag{A15}$$

Let $K_I'(R,\phi,t_1)$ be calculated using

$$K_I'(R,\phi,t_1) = \frac{\sigma_{zz}(R,\phi,t_1)R^{1/2}}{f_{-1/2}(\phi)} \quad . \tag{A16}$$

Substitute equation (A16) into (A15).

$$K_I'(R,\phi,t_1) = K_I(t_1) - \frac{f_{1/2}(\phi,t_1)R}{f_{-1/2}(\phi)}$$

$$- \frac{1}{f_{-1/2}(\phi)} \left(f_0(\phi,t_1)R^{1/2} + f_1(\phi,t_1)R^{3/2} + f_{3/2}(\phi,t_1)R^2 \right.$$

$$\left. + f_2(\phi,t_1)R^{5/2} + \mathbf{O}(R^3) \right) \tag{A17}$$

Equation (A17) may approximated to be a linear function in R using

$$K_I'(R,\phi,t_1) = K_I(t_1) + mR \quad , \tag{A18}$$

where m is a constant. Values of $K_I'(R,\phi,t_1)$ are calculated at different points from $\sigma_{zz}(R,\phi,t_1)$ computed from the finite element analysis. The coefficient $K_I(t_1)$ is the desired dynamic stress intensity factor and can then be obtained by performing a least squares linear curve fit [56] to these points. As the terms inside the large brackets in equation (A17) were neglected the linear extrapolation to $K_I(t_1)$ introduced an error in $K_I(t_1)$ of $\mathbf{O}((R/a)^{1/2})$. However, by setting $\phi = 0$, the property given by equation (A14) reduces this extrapolation error to $\mathbf{O}((R/a)^2)$. Additional error will arise from that in the numerical solution for $\sigma_{zz}(R,\phi,t_1)$.